



# Syn-kinematic hydration reactions, dissolution-precipitation creep and grain boundary sliding in experimentally deformed plagioclase - pyroxene mixtures

Sina Marti<sup>1</sup>, Holger Stünitz<sup>2,3</sup>, Renée Heilbronner<sup>1</sup>, Oliver Plümper<sup>4</sup>, and Rüdiger Kilian<sup>1</sup>

<sup>1</sup>Department of Environmental Sciences, Basel University, Switzerland

<sup>2</sup>Department of Geosciences, UiT the Arctic University of Norway, Norway

<sup>3</sup>Institut des Sciences de la Terre d'Orléans (ISTO), Université d'Orléans, France

<sup>4</sup>Department of Earth Sciences, Utrecht University, The Netherlands

**Correspondence:** Sina Marti ([sina.marti@ed.ac.uk](mailto:sina.marti@ed.ac.uk))

**Abstract.** While it is widely observed that mafic rocks are able to experience high strains by viscous flow, details on their rheology and deformation mechanisms are poorly constrained. Here, rock deformation experiments on four different, water-added plagioclase-pyroxene mixtures are presented: (i) plagioclase(An60-70) – clinopyroxene – orthopyroxene, (ii) plagioclase(An60) – diopside, (iii) plagioclase(An60) – enstatite and (iv) plagioclase(An01) – enstatite. Samples were deformed in  
5 general shear at strain rates of  $3 \cdot 10^{-5}$  to  $3 \cdot 10^{-6} \text{ s}^{-1}$ , 800 °C and confining pressure of 1.0 or 1.5 GPa. Results indicate that dissolution-precipitation creep (DPC) and grain boundary sliding (GBS) are the dominant deformation mechanisms. Coinciding with sample deformation, syn-kinematic mineral reactions yield abundant nucleation of new grains; the resulting intense grain size reduction is considered crucial for the activity of DPC and GBS. In high strain zones dominated by plagioclase, a weak, non-random and geometrically consistent crystallographic preferred orientation (CPO) is observed. Usually, a CPO is  
10 considered a consequence of dislocation creep, but the experiments presented here demonstrate that a CPO can develop during DPC and GBS. This study provides new evidence for the importance of DPC and GBS in mid-crustal shear zones within mafic rocks, which has important implications on understanding and modelling of mid-crustal rheology and flow.

## 1 Introduction

15 Viscous deformation of crustal rocks is usually dominated either by intra-crystalline deformation (dislocation creep), or by mechanisms such as diffusion creep and grain boundary sliding. Apart from being rate and temperature sensitive, the rheology of viscously deforming rocks is also observed to be material dependent (for a comprehensive list of flow law parameters for different rock types see e.g., Kohlstedt et al. (1995); Shaocheng and Bin (2002); Bürgmann and Dresen (2008); Burov (2011) and references therein). Flow laws for viscous creep exist for different types of rocks, with the majority of these flow laws  
20 being determined for monomineralic materials. It is often suggested that viscous deformation in monomineralic aggregates at



mid- to lower crustal conditions is dominated by dislocation creep. Grain growth in monomineralic aggregates at the elevated temperatures of the mid- to lower crust is assumed to be extensive and the resulting large grain size is expected to render diffusion creep less efficient than dislocation creep. Insights into deformation mechanisms, slip systems, and flow law parameters have been obtained from experimental studies, e.g., for plagioclase: Tullis and Yund (1985); Shaocheng and Mainprice (1987);  
25 Tullis and Yund (1991); Dimanov et al. (1999); Rybacki and Dresen (2000); Stünitz and Tullis (2001); Stünitz et al. (2003); Ji et al. (2004); Barreiro et al. (2007), and for pyroxene: Lallemand (1978); Kolle and Blacic (1982); Raterron and Jaoul (1991); Mauler et al. (2000); Bystricky and Mackwell (2001); Hier-Majumder et al. (2005); Chen et al. (2006); Zhang et al. (2006). For polyphase mixtures of gabbroic composition, data from high-temperature deformation experiments are published by Dimanov et al. (2003, 2007); Dimanov and Dresen (2005). Depending on the grain size, the differential stress and the volume  
30 fraction of pyroxene (as the stronger phase in their pyroxene-plagioclase mixtures), the dominant deformation mechanism identified by these authors is either diffusion creep or dislocation creep. The strain rate of the two-phase aggregates thereby is suggested to be a combination of the strain rates of the individual phases e.g., Dimanov et al. (2003). No mineral reactions were observed in these experiments.

In somewhat lower-temperature experiments and mostly under hydrous conditions, Rutter et al. (1985); Getsinger and Hirth  
35 (2014), and Stünitz and Tullis (2001) performed deformation experiments with syn-kinematic hydration reactions. Phase mixing was found to be (partly) due to the nucleation of new phases. The authors suggest that the dominant deformation mechanism is grain size sensitive creep by a mix of diffusion creep and grain boundary sliding. Rutter et al. (1985) state explicitly that they interpret diffusion creep in the sense of dissolution-precipitation creep.

In polymineralic mixtures, several processes are known to influence the deformability and the dominating deformation mechanism of the bulk aggregate. The occurrence of mineral reactions and nucleation causes grain size reduction (e.g., Brodie and  
40 Rutter, 1987; Fitz Gerald and Stünitz, 1993; Newman et al., 1999; de Ronde et al., 2005) and can lead to (further) phase mixing. Grain pinning due to secondary phases will impede grain growth (e.g., Olgaard and Evans, 1986; Berger and Herwegh, 2004; Linckens et al., 2011), and diffusion is expected to be faster along phase boundaries compared to grain boundaries (e.g. Hickman and Evans, 1991; Wheeler, 1992; Sundberg and Cooper, 2008). These factors enhance diffusion creep rates and thus  
45 may lead to a switch of the dominant deformation mechanism from dislocation creep in monomineralic layers, to diffusion creep in polymineralic layers (Etheridge and Wilkie, 1979; Mehl and Hirth, 2008; Linckens et al., 2011; Kilian et al., 2011).

In the absence of fluids, metastable mineral assemblages can be preserved over long time periods (e.g., Jamtveit et al., 2016). When fluids infiltrate, mineral reactions take place. Under deviatoric stress conditions, deformation is frequently localized along these zones of fluid infiltration and metamorphic reactions (e.g., Austrheim, 1987). A positive feedback between deformation and metamorphic reactions has been recognized for some time but the exact mechanisms of the interaction are still  
50 not sufficiently understood. The positive feedback with metamorphic reactions may not be the same for all deformation mechanisms and thus the syn-kinematic occurrence of mineral reactions is a factor that can influence the dominance of a certain deformation mechanism.

In the presence of fluids, mafic rocks are particularly susceptible to reactions during changing temperatures and pressures,  
55 representing a suitable material to study the interplay between reaction and deformation. That high strain zones such as ul-



tramylonites usually consist of a phase mixture, indicates their ability to deform at higher strain rates (or lower stresses) than monomineralic aggregates and emphasizes their importance for localizing deformation.

In this study, we present results from deformation experiments on water-added plagioclase-pyroxene mixtures. At the imposed pressure-temperature conditions of  $\sim 1.0 - 1.5$  GPa and  $800$  °C, deformation takes place within the lower temperature range  
60 of the viscous regime. The metastability of the starting material in the  $H_2O$ -present system causes syn-kinematic mineral reactions, thus facilitating the interplay between reaction and deformation in the experiments.

## 2 Materials and Methods

### 2.1 Experiments

#### 2.1.1 Starting materials

65 Experiments are performed on five different starting materials (composition of starting material and chemical composition of minerals are given in Table 1; mineral abbreviations after Whitney and Evans (2010)):

- (i) MD: Crushed Maryland Diabase, (Kronenberg and Shelton, 1980; Marti et al., 2017), using a grain size fraction  $\leq 125$   $\mu\text{m}$ . The Maryland Diabase starting material has a modal composition of plagioclase:  $\sim 57$  vol%, Clinopyroxene:  $\sim 32$  vol%, Orthopyroxene:  $\sim 8$  vol%, Accessories:  $\sim 3$  vol% (Qz, Kfs, Ilm, Mag, Bt, Ap).
- 70 (ii) An60+En: Synthetic mixture of Sonora labradorite ( $\sim$  An60) and Damaping enstatite. powder. Grain size fraction of  $\sim 2 - 125$   $\mu\text{m}$ , and  $40 - 180$   $\mu\text{m}$ .
- (iii) An60+Di: Synthetic mixture of Sonora Labradorite and Damaping diopside (D) powder. Grain size fraction of  $\sim 2 - 125$   $\mu\text{m}$ .
- (iv) An60+Di: Synthetic mixture of Sonora labradorite and Cranberry Lake diopside powder. Grain size fraction of  $\sim 2 - 125$   
75  $\mu\text{m}$ , and  $40 - 125$   $\mu\text{m}$ .
- (v) Ab+En: Synthetic mixture of Alpe Rischuna albite ( $\sim$  Ab98) and Damaping enstatite powder. Grain size fraction of  $\leq 125$   $\mu\text{m}$ , and  $40 - 180$   $\mu\text{m}$ .

Detailed description of the sample preparation can be found in the Appendix. Synthetic plagioclase-pyroxene powders are mixed with phase proportions of  $\sim 57$  vol% plagioclase to  $43$  vol% pyroxene. Either  $0.2$   $\mu\text{l}$  ( $0.18$  wt%) or  $0.12$   $\mu\text{l}$  ( $0.11$  wt%)  
80  $H_2O$  is added to the sample.

#### 2.1.2 Experimental conditions and sample assembly

Experiments are performed using the Griggs-type deformation apparatus at the University of Tromso, Norway. Experiments are run at confining pressures ( $P_c$ ) of  $\sim 1.0$  and  $1.5$  GPa, temperatures ( $T$ ) of  $800$  °C and (axial) displacement rates of  $\sim$



2·10<sup>-8</sup> to 2·10<sup>-9</sup> ms<sup>-1</sup> resulting in bulk strain rates of  $\sim 3\cdot 10^{-5}$  to  $3\cdot 10^{-6}$  s<sup>-1</sup>. General shear type of flow is achieved by placing  
85 the rock powder (0.11 g) between cylindrical alumina forcing blocks (diameter of 6.33 mm) pre-cut at 45° with respect to the  
load axis (Appendix Figure A.1). Descriptions of the experimental setup, data recording and data treatment can be found in the  
Appendices A1 - A3, experimental conditions are listed in Table 2.

## 2.2 Strain determination

The thickness of the shear zone at the hit-point is  $th_0 = 0.75 \pm 0.03$  mm. During the experiment,  $\sim 86 \pm 3$  % of the axial  
90 displacement is accommodated as shear displacement within the shear zone, and  $\sim 14 \pm 3$  % is accommodated as plane strain  
thinning of the shear zone. As in previous experiments, the shear zone thickness decreases linearly with the applied axial  
displacement (see Marti et al., 2017).

The shear strain is presented as apparent shear strain,  $\gamma_a$ , and calculated as the sum of the incremental shear displacements  
divided by the instantaneous shear zone thickness and strain rates are given as apparent shear strain rates,  $\dot{\gamma}_a$ , (see Marti et al.  
95 2017).  $\gamma_a$  is calculated for the full width of the shear zone ignoring any strain localization. Since  $\gamma_a$  overestimates the shear  
strain and cannot be used to determine the strain ellipsoid or other strain related parameters, the procedure described by Fossen  
and Tikoff (1993); Tikoff (1995) is adopted. Table 2 lists the simple shear ( $\gamma$ ) and pure shear (k) components, as well as the  
orientation of the instantaneous stretching axes (ISA), the orientation of the finite stretching direction, the kinematic vorticity  
number and the strain ration given by the ratio of long to short axis of the strain ellipsoid.

## 100 2.3 Image analysis

After the experiments, samples are immersed in epoxy, cut parallel (in some cases also normal to the shear direction), and  
prepared to polished thin sections. Polarized light microscope, scanning electron microscope (SEM) and transmission electron  
microscope (TEM) are used for sample analysis. Grain size and surface fabric are determined as described in Appendix A5.

A special method is developed to study the amphibole coronas that grow on pyroxene porphyroclasts. Corona thickness is  
105 measured as a function of orientation around the clasts (Figure 1). To this end, phase maps of pyroxene and amphibole are  
created (as described in Appendix A5). Where amphibole coronas of neighboring pyroxene clasts are in contact, individual  
pyroxene - amphibole pairs have to be separated manually. Clean phase maps contain segmented pyroxene and amphibole  
phases, and each pyroxene grain is in contact only with its own amphibole corona. The x-y coordinates of the clast (pyroxene)  
and the aggregate (pyroxene + corona) outlines are measured and exported using Fiji and a modified version of the *Jazy XY*  
110 *export macro* (by Rüdiger Kilian, available at <https://earth.unibas.ch/micro/index.html>). Using a MATLAB script (available  
from the author upon request), the x-y coordinates of clast and aggregate outlines are converted to polar coordinates ( $r-\theta$ ), and  
the corona thickness,  $thc(\theta)$ , is determined at each point along the pyroxene clast as the shortest distance between the clast to  
the aggregate outline (Figure 1c) as a function of  $\theta$ . The angle runs counter clock wise from the horizontal. This approach yields  
good results where coronas follow the clast shape, but tends to underestimate corona thickness where the corona becomes very  
115 elongated as e.g. in 'tails' around the clasts. Note that where tails grew extensively long, they were eventually cut, so that the  
analysis does not include the whole tail length (Figure 1b).



### 3 Results

#### 3.1 Mechanical data

For all experiments, the mechanical data plotted as shear stress,  $\tau$ , vs. apparent shear strain,  $\gamma_a$ , show a curve with an initial  
 120 steep increase of shear stress, reaching a peak value usually after  $\sim \gamma_a$  of 0.8 - 1.0 (Figure 2). Peak stress is followed by a slow  
 decrease, often approaching a quasi-steady state shear stress value from  $\gamma_a \approx 4$  onwards. The samples with 0.12  $\mu\text{l}$   $\text{H}_2\text{O}$  added  
 show higher peak stresses and a more rapid shear stress decrease thereafter, compared to samples with 0.2  $\mu\text{l}$   $\text{H}_2\text{O}$  added. For  
 the Maryland Diabase samples (Figure 2a) at  $P_c \approx 1.0$  GPa, the sample with 0.12  $\mu\text{l}$   $\text{H}_2\text{O}$  reaches a higher peak stress, but after  
 an additional  $\sim 0.5 \gamma_a$ , it drops to a value similar to the samples with 0.2  $\mu\text{l}$   $\text{H}_2\text{O}$ . Sample strength of Maryland Diabase at 1.0  
 125 and 1.5 GPa reach the same peak stress, but the 1.0 GPa experiments weaken more rapidly within the attained strain range.

The synthetic plagioclase-pyroxene mixtures (Figure 2b) show similar peak stress values (460 - 530 MPa) and all but the  
 An60+En mixture attain similar flow stresses. The synthetic mixtures generally support  $\sim 60$  - 110 MPa higher shear stresses  
 than the Maryland Diabase samples (compare Figure 2a and b). At peak stress, the synthetic mixtures (samples 503, 518 and  
 519) reach differential stress values near the Goetze criterion. According to Kohlstedt et al. (1995), the Goetze criterion,  $\Delta\sigma$   
 130  $\leq P_c$ , is an empirically defined stress range where rocks are expected to deform plastically. However, due to the significant  
 weakening subsequent to peak stress, many samples which start above the Goetze criterion then fall substantially below it. The  
 Maryland Diabase samples all stay below the Goetze criterion for all stages of deformation.

Strain rate stepping tests on Maryland Diabase sample material at  $P_c \approx 1.0$  and 1.5 GPa have been performed (Figure 2c).  
 Stress exponents,  $n$ , of  $n = 1.9$  and  $n = 1.4$  are obtained for experiments at  $P_c \approx 1.0$  and 1.5 GPa respectively (Figure 3).

#### 135 3.2 Microstructures

In all experiments strain is partitioned into a network of shear bands (Figure 4, Figure 5). Their thickness is variable but the  
 main shear band strands usually have a thickness on the order of 40 - 150  $\mu\text{m}$  (e.g. Figure 5d, j) and are characterised by strong  
 grain size reduction (Figure 5b, e, k).

The following hydration reactions are observed within shear bands and in low strain lenses:

140



where  $Pl_2$  has a lower anorthite component than  $Pl_1$ .

145 In Maryland Diabase samples, both reaction (R1) and (R2) occur pervasively, with reaction (R1) being the more prominent  
 one. Amphibole grows as reaction coronas on pyroxene clasts and as aggregates, often mixed with quartz, inside shear bands  
 (Figure 5b, Figure 6a, c). The volume of hydrous reaction products reaches about 15 - 25 % for experiments with durations



of  $\sim 60 - 70$  h (lead run-in and subsequent deformation to  $\gamma_a \approx 4$  to 6). Shear bands in Maryland Diabase experiments are broad and subparallel to the shear zone boundaries (Figure 5c), with an angle  $\phi = 3^\circ$  between the preferred orientation of shear bands and shear zone boundaries (see Figure 5 for reference frame). Shear bands are mainly formed by grains with  $< 1$   $\mu\text{m}$  diameter and frequently show a compositional layering between plagioclase dominated and amphibole dominated layers (Figure 5b, Figure 6a, b). Plagioclase layers are either monomineralic or show mixing with zoisite. In amphibole dominated layers, amphibole is frequently occurring together with quartz. Mixing between amphibole and plagioclase is subordinate.

In synthetic mixtures of An60+En and An60+Di mixtures (Figure 5d - i), (R2) is the dominant hydration reaction. The volume of hydrous reaction products reaches 1- 9 % for experiments with durations of  $\sim 66 - 69$  h (lead run-in and subsequent deformation). In the An60+En mixture, shear bands are somewhat narrower and more anastomosing. At an angle,  $\phi = 9^\circ$ , they are also more inclined to the shear zone boundaries compared to the other samples (Figure 5f). Shear bands in both, An60+En and An60+Di mixtures are mainly formed by fine-grained ( $< 1\mu\text{m}$ ) plagioclase and zoisite.

The zoisite reaction predicts the formation of a new plagioclase with a lower anorthite component. The fine grain size within shear bands does not allow for quantitative EDS measurements, but Back-scattered Electron (BSE) images reveal lower Z-contrast (= lower anorthite contents) for plagioclase within shear bands compared to plagioclase porphyroclasts (Figure 5e). Semi-quantitative EDS measurements yield a decrease in anorthite component from  $\sim \text{An}(60)$  (starting composition) to  $\sim \text{An}(52-55)$  for grains within shear bands (Figure 7).

In the Ab+En sample, shear bands are broad and sub-parallel to the shear zone boundaries, with  $\phi = 6^\circ$  (Figure 5l). Shear bands are pre-dominantly composed of fine-grained plagioclase (Figure 5k) with sizes  $< 2 \mu\text{m}$ . No difference in composition between plagioclase porphyroclasts and fine-grained plagioclase within shear band was detected. In high-resolution BSE images, a fine-grained phase with a Z-contrast similar to enstatite is observed. Due to the small grain size EDS measurements are extremely challenging but point to a new type of pyroxene with a somewhat higher Si and Na component.

In all experiments (Maryland Diabase and synthetic mixtures), plagioclase shows extensive grain size refinement. Porphyroclasts are replaced by fine-grained plagioclase, nucleating mainly along porphyroclast rims and along straight internal trails, which are thought to represent former fractures (Figure 5k). The newly nucleated grains generally show a lower anorthite component than the plagioclase in the starting material (Figure 7). In experiments on Maryland Diabase, pyroxene grain size reduction is largely caused by the pyroxene-consuming reaction to Amp (R1, Figure 5b, Figure 6). In the synthetic mixtures however, much of the grain size reduction of pyroxene is caused by fracturing.

The main difference between the microstructures developed at 1.0 and 1.5 GPa Pc (Maryland Diabase experiments) is the increased amount of reaction products at higher Pc (Figure 6). Zoisite and amphibole form more abundantly at 1.5 GPa and amphibole corona surround pyroxene porphyroclasts in early stages of the experiments. Shear bands at Pc  $\approx 1.0$  GPa are mainly composed of a fine-grained mixture of Pl+Am+Qz+Zo (in order of abundance), as compared to Amp+Pl+Zo+Qz (again in order of abundance) at 1.5 GPa. Additionally, shear bands are somewhat narrower and more inclined to the shear zone boundaries at the higher Pc (compare Marti et al., 2017).



### 3.3 Amphibole chemistry

For Maryland Diabase experiments at 1.0 GPa, two groups of amphibole are recognized, differing in their Al and Mg per  
185 formula unit (p.f.u.), and in their Na to Al ratio (Figure 8, Table 3, Supplementary Table 1). The amphiboles are classified  
as ranging between Tschermakite and Mg-Hornblende. When labelling the amphibole measurements according to their 2D  
neighbourhood as observed in the thin section, the Al and Mg contents shows a consistent pattern where high Al - low Mg  
amphibole grow in plagioclase dominated areas (Figure 8b - d). The Si and Ca contents thereby show no systematic difference  
between the different grain neighbourhoods. Supplementary Table 1 lists amphibole and plagioclase (starting material and  
190 newly nucleated) compositions.

Two groups of amphibole compositions are present, which can be distinguished by their Na per Al content ratio (Figure 8e,  
f). The plagioclase of the Maryland Diabase starting material has an anorthite component of  $\sim$  An(65-70), with thin rims of  
 $\sim$  An(52-56) (Figure 7). The core's Na to Al ratio thus is  $\sim$  0.18 - 0.21. Plagioclase is the sole provider for Na and Al in  
amphibole as pyroxene in the starting material shows only trace amounts of these elements. Most amphibole measurements  
195 show an Na:Al-ratio of 0.16 - 0.21 (Figure 8f), consistent with reaction (R1) and the consumption of a plagioclase with a  
composition of  $\sim$  An(65-70). The second type of amphibole, with Na:Al-ratios  $>$  0.25 is comparable to the Na:Al-ratio of the  
starting plagioclase rim composition of  $\sim$  An(52-56) (resulting in Na:Al-ratios of  $\sim$  0.28 - 0.32) and thus again would be  
compatible with the plagioclase-consuming, amphibole forming reaction (R1).

### 3.4 Shear bands

#### 200 3.4.1 Nanostructure of plagioclase within shear bands

TEM images are presented from shear bands formed within the Ab+En sample 518 (Figure 9) and the Maryland Diabase  
sample 414 (Figure 10). For both samples, micrographs are obtained from foils cut normal to the shear zone boundaries and  
parallel to the shear direction. Figure 9a shows the interface between an albite porphyroclast and the fine-grained albite matrix  
of an adjacent shear band. The albite clast has a high defect density, where intergranular domains develop misorientations to  
205 each other, as seen in the bright field image or from the rotation of diffraction spots (Figure 9b). However, no recovery to  
form sub-grain walls is observed. Furthermore, the interface between the clast and the shear band is sharp and no bulges are  
observed (Figure 9a). Within the shear band, small pores are seen as pore trails along grain boundaries (Figure 9c, d) oriented  
at a small angle to the expected  $\sigma_1$ .

The shear band formed in the Maryland Diabase sample shows the typical compositional layering between plagioclase domi-  
210 nated layers and amphibole (+Qz) aggregates (Figure 10a). Bright field TEM images reveal largely defect free grains (Figure  
10b, d) and grain sizes are similar for amphibole and plagioclase. Grain and phase boundaries are tight and porosity is scarce  
(Figure 10c, d). Plagioclase grains are weakly anisotropic in shape (not perfectly equant) with a shape preferred orientation  
sub-parallel to the shear zone boundaries (Figure 10b, d; compare Marti et al., 2017).



### 3.4.2 Plagioclase grain size distribution within shear bands

215 2D grain size distributions (GSDs) are determined for plagioclase inside shear bands of the Ab+En experiment 518 and the MD experiment 414 (Figure 11). The distributions in the two samples are similar with somewhat higher frequencies in bins  $> 1 \mu\text{m}$  for albite compared to the labradorites of the Maryland Diabase sample. Due to the small grain sizes and extremely narrow grain boundaries, grains are difficult to identify on SEM images and there is some uncertainty concerning the measured GSDs inherent from the grain segmentation. Nonetheless, grains segmented from TEM and SEM images correlate well for the highest frequency bins. Measured on TEM and SEM images, the GSDs for sample 518 have modes at 0.51 and 0.36  $\mu\text{m}$  respectively. In sample 414, the GSDs have modes at 0.23 and 0.30  $\mu\text{m}$  (Figure 11).

### 3.4.3 Albite crystallographic preferred orientation

Three EBSD maps are collected along one shear band in the Ab+En sample 518 (Figure 12). Orientation data of plagioclase grains with  $< 2 \mu\text{m}$  equivalent diameter are plotted in pole figures for [100], [010] and [001], as well as poles to (010)-planes. Orientation data of porphyroclasts and their fractured fragments is excluded. Although J-indices indicate only weak crystallographic preferred orientations (CPO) in the different sites, the CPO patterns are similar in all three sites. Poles to (010) planes tend to be oriented near the periphery with a large angle to the trace of the shear band plane. [100] axes show peripheral and central maxima, not far from the trace of the shear band plane. The EBSD map in site2 contains a large plagioclase porphyroclast and the orientation data of this clast is plotted in the pole figures of this site (Figure 12a). The porphyroclast orientation does not show a systematic relationship with the maxima of the orientations measured from the  $< 2 \mu\text{m}$  shear band grains.

## 3.5 Amphibole coronas

Amphibole grows abundantly in experiments on Maryland Diabase, especially at the higher Pc (e.g. Figure 6c), where pyroxene clasts are surrounded by amphibole coronas already in early stages of the experiment. Pyroxene clast - amphibole rim pairs from experiments performed at Pc  $\approx 1.5$  GPa were analysed, studying the average amphibole corona thickness as a function of orientation around pyroxene porphyroclasts (Figure 13). Coronas are measured at three different stages: at hydrostatic conditions ( $\Delta\sigma \approx 0$ ), at peak stress ( $\Delta\sigma > 0$ ;  $\gamma_a \approx 1$ ) and after considerable deformation ( $\Delta\sigma > 0$ ;  $\gamma_a \approx 4$ ) corresponding to three evolutionary stages of a typical high strain experiment (Appendix Figure A.1c). Accordingly, three cases are distinguished. The *hydrostatic* case represents the microstructural state at the hit-point after the lead run-in. The *peak stress* case records the microstructural state at the time the sample has reached its maximum strength (including lead run-in and initial sample loading) and the *deformed* case represents the microstructure evolved after the sample underwent high shear strain (including lead run-in, sample yielding and deformation; for an explanation on the nomenclature used see Appendix Figure A.1c).

At hydrostatic conditions (e.g. during the lead run-in), corona growth is symmetrical around the clasts, with an average thickness of 2.4 to 3.1  $\mu\text{m}$  (Figure 13a). In the *deformed* case, the average corona thickness shows an overall monoclinic shape. Assuming that the microstructure after lead run-in (hydrostatic part) is approximately the same as that of the *hydrostatic* case



sample, the corona thickness in the *deformed* sample is reduced by  $\sim 0.5 - 2 \mu\text{m}$  in directions close to the loading direction. Thickness is reduced in most directions except in the range of  $346^\circ - 53^\circ$  and  $186^\circ - 232^\circ$ , where it is increased. That is, on average, the corona thickness is reduced on clast surfaces facing the loading direction, and increased at high angles to the loading direction. At *peak stress* the average corona thickness in direction of loading is the same as in the *hydrostatic* case ( $\sim$  250  $2.7 \mu\text{m}$ ) but already increased in almost all other directions. Furthermore, despite the 23 h longer duration of the *hydrostatic* run compared to the *peak stress* run (Figure 13c), coronas did not grow to larger thicknesses in the former.

Instantaneous stretching and shortening axes (ISA), finite stretching directions and vorticity numbers ( $W_k$ ) are calculated for the *peak stress* and the *deformed* case (Figure 13b). The orthorhombic shape of the peak stress corona curve is well described by the ISA, e.g., such that the long side is normal to the shortening ISA. After deformation, the long diameter of the monoclinic 255 shaped corona curve is oriented between the stretching ISA and the finite stretching direction. The short diameter corresponds to the shortening sector around the pyroxene clast. The direction of the maximum corona thickness is at a higher angle with respect to the shear plane than the finite stretching direction (Figure 13b).

## 4 Discussion

### 4.1 Physics and chemistry of grain size reduction

260 There is a drastic grain size decrease (down to diameters  $< 2 \mu\text{m}$ ) accompanied with the shear band formation (Figure 5, Figures 9-11). Fracturing as an important process of grain size reduction is only observed in pyroxene grains of the synthetic mixtures (e.g. Figure 12b). In these samples, pyroxene only participates in mineral reactions to a minor degree, and the plagioclase hydration reaction (R2) is dominating (except for the Ab+En sample). In contrast, pyroxene grains in experiments on Maryland Diabase show grain size reduction by dissolution during the pyroxene-consuming reaction (R1) to amphibole.

265 Fracturing only minorly contributes to the grain size reduction of plagioclase. Instead, grain size reduction is primarily caused by mineral reactions and abundant nucleation of new grains. New plagioclase grains have a different composition from that of the original clasts (e.g. Figure 7). The low defect densities, the narrow grain size range, and the lozenge shaped grains of the very fine-grained pure plagioclase aggregates within shear bands (Figures 9-11) are in accordance with a formation by nucleation and limited growth. Of the two initial mineral phases, plagioclase and pyroxene, plagioclase is particularly susceptible to 270 grain size reduction via reaction and nucleation of new grains. For all new phases, like zoisite and amphibole, it is clear that reaction and nucleation are the mechanisms leading to a small grain size and to phase mixing.

In the special case of the Ab+En experiment, it is difficult to observe an obvious change in chemical composition of the plagioclase and to connect it to grain size reduction in shear bands. Qualitative EDX measurements reveal possible new pyroxene grains with higher Si and Na contents compared to the starting pyroxene. Due to the very small grain size, however, chemical 275 measurements are challenging. No measurable change in plagioclase composition is detected but in order for the new pyroxene to grow with higher Si and Na contents compared to the starting material, a plagioclase with a higher anorthite component is expected to grow.

Microstructural evidence for grain size reduction by fracturing or dynamic recrystallization (e.g. subgrain rotation or bulging



recrystallization) of plagioclase is not observed (see e.g. Figure 9). In addition, had the recrystallization of plagioclase in  
280 monomineralic domains taken place by dynamic recrystallization, the resulting grain sizes would imply very high stresses.  
Using the normalized grain size/stress relationship by Derby (1991), the observed plagioclase grain size mode of  $\sim 0.4 \mu\text{m}$   
(Figure 11) would require differential stresses of 2 to 2.5 GPa. The observed differential stresses are  $\sim 500 \text{ MPa}$  in the last  
stages of this experiment (Figure 2) - they are clearly far too low to produce such a small grain size in equilibrium. As in  
other samples, grain size reduction of plagioclase in the Ab+En sample is considered to take place by dissolution of original  
285 porphyroclasts and nucleation (i.e. "neo-crystallization") of new grains.

#### 4.2 Derivation of the stress exponent

The determined  $n$ -values are low, with  $n = 1.4$  and  $1.9$  (Figure 3) and are thus within the range of expected values for diffusion  
creep (including grain boundary sliding) with theoretical values between 1 (e.g., Ashby and Verrall, 1973; Coble, 1963; Karato,  
2008; Kohlstedt and Hansen, 2015; Paterson, 2013), up to 2 (e.g., Gratier et al., 2009, 2013; Paterson, 2013). The stress  
290 exponents determined in this study have to be taken with some caution as deformation of the samples is inhomogeneous.  
While the shear bands are able to accommodate higher strain rates, the lesser deformed domains between seem to still control  
the overall bulk stress (Marti et al., 2017). Nevertheless, the low stress exponents strongly suggest an absence of frictional  
deformation and make dislocation creep unlikely.

#### 4.3 Albite crystallographic preferred orientation

295 Dislocation creep and dynamic recrystallization are not considered to occur in our experiments. The large Burgers vectors and  
the cation ordering (coupled Al+Ca and Si+Na) in plagioclase are unfavourable for intracrystalline deformation, especially at  
the comparatively low experimental temperatures of  $800 \text{ }^\circ\text{C}$ .

Dislocation glide and climb have been suggested to be active in plagioclase at both natural and experimental conditions (e.g.,  
Tullis and Yund, 1985; Shaocheng and Mainprice, 1987; Yund and Tullis, 1991; Rybacki and Dresen, 2000; Shigmeatsu and  
300 Tanaka, 2000; Kruse et al., 2001; Lapworth et al., 2002; Stünitz et al., 2003; Ji et al., 2004; Barreiro et al., 2007; Mehl and  
Hirth, 2008) but usually are not considered to accommodate large amounts of strain. Recrystallization takes place by different  
mechanisms including neo-crystallization (e.g., Fitz Gerald and Stünitz, 1993; Rosenberg and Stünitz, 2003; Brander et al.,  
2012; Fukuda and Okudaira, 2013; Mukai et al., 2014) or by growth of fragments formed by fracturing (e.g., Stünitz et al.,  
2003; Viegas et al., 2016). In fine-grained aggregates, diffusion creep (in the broadest sense) often dissolution-precipitation  
305 creep (DPC), is the main strain accommodating process described for polycrystalline plagioclase aggregates (e.g., Yund and  
Tullis, 1991; Fitz Gerald and Stünitz, 1993; Jiang et al., 2000; Lapworth et al., 2002; Rosenberg and Stünitz, 2003; Brander  
et al., 2012; Fukuda and Okudaira, 2013; Mukai et al., 2014; Viegas et al., 2016).

The CPO measured in a shear band of the Ab+En sample 518 is generally weak, but the three independent sites 1 - 3 show  
very similar CPO patterns (Figure 12). This similarity indicates that these CPOs, although weak, are not random but that there  
310 must be a mechanism leading to this weak but consistent CPO.

There are a number of mechanisms that can lead to a CPO within an aggregate. Examples are dislocation glide (e.g., Schmid



and Boas, 1950) or directed growth (possibly together with rigid body rotation; e.g. Shelley, 1994; Berger and Stünitz, 1996; Rosenberg and Stünitz, 2003; Getsinger and Hirth, 2014; Viegas et al., 2016). Furthermore, a CPO can form due to interfacial energy, e.g., via host-controlled nucleation (e.g., Jiang et al., 2000) or caused by interface-controlled diffusion creep (e.g., Bons and den Brok, 2000; Sundberg and Cooper, 2008). Similar CPOs as the ones shown here have been found in experimentally deformed anorthite and basalt (e.g., Ji et al., 2004; Barreiro et al., 2007), and in naturally deformed basaltic and peridotitic rocks (e.g., Mehl and Hirth, 2008; Viegas et al., 2016; Xie et al., 2003; Drury et al., 2011). Ji et al. (2004) and Mehl and Hirth (2008) interpret the CPOs to be due to dislocation creep in monomineralic plagioclase layers. Viegas et al. (2016) observe no evidence for dislocation creep and suggest that the CPOs may be the result of directed growth and rigid body rotation of grains (with a crystallographically controlled grain shape) during diffusion accommodated grain boundary sliding. In our case, we observe no microstructural evidence for dislocation creep and suggest that the observed CPOs did not form as a consequence of intracrystalline plasticity (see also section 4.5).

#### 4.4 Evidence for dissolution-precipitation creep of amphibole

During the experiments, amphibole grows as a reaction product and pyroxene porphyroclasts are replaced at their rims by amphibole growth coronas. During all stages of an experiment, amphibole is observed to grow stably. However, the amphibole coronas, which grow symmetrically in thickness during the hydrostatic 'lead run-in', become partly dissolved in high stress sites while simultaneously growing thicker in low stress sites during deformation (Figure 13a). These results indicate grain scale DPC of amphibole. DPC is a form of diffusion creep in the presence of an aqueous fluid. It is frequently observed for amphiboles in naturally deformed rocks (e.g., Berger and Stünitz, 1996; Imon et al., 2002; Marsh et al., 2009; Stokes et al., 2012), but has only rarely been reproduced in experimental studies (Rutter et al., 1985; Getsinger and Hirth, 2014).

The direction of the shortening ISA (equal to the direction of the instantaneous maximum principal stress,  $\sigma_1$ ) lies within the range of directions of minimum average corona thickness. A correlation between the shortening ISA and the minimum in average corona thickness is consistent with the interpretation of DPC, where material is preferentially dissolved along high stress sites (and re-precipitated along low stress sites). The geometry of deformation by diffusion creep is irrotational (Karato, 2008), that is, as the principal stress axes are normal to each other, the resulting (grain shape) fabric due to diffusion creep should be orthorhombic. At the *peak stress*, where shear strain is still small, the rim thickness shows an overall  $\sim$  orthorhombic shape (see corona curve in Figure 13b), well aligned with the ISAs. As the ISAs should indicate the minimum and maximum principle stress directions, the fact that the corona curve follows the ISAs correlates well with the interpretation that DPC determines the amphibole corona thickness evolution. The monoclinic shape of the corona curve in the *deformed* case can be explained by a superposition of co-axial geometry of deformation by diffusion creep, and rigid body rotation induced by the rotational component of simple shear.

Clasts with coronas are predominantly found in low strain lenses, where shear strains are lower than in shear bands. No microstructure can be found to indicate that the reduction in average corona thickness at the compressional sites of the clasts is due to 'shearing-off' of amphibole from compressional to extensional sites by some sort of granular flow.



#### 345 4.5 Dissolution-precipitation creep and grain boundary sliding

From the mechanical data (including stress exponents), the determined grain sizes, from the nucleation of new grains, and from amphibole growth fabrics discussed above, it is concluded that in all samples, the dominant deformation mechanism cannot be frictional or crystal plastic (dislocation creep). Instead, the dominant deformation mechanisms for amphibole and plagioclase are inferred to be DPC (accompanied and/or accommodated by mineral reactions) and grain boundary sliding. Pyroxene is less  
350 involved in accommodating strain but plays an important part by being involved in mineral reactions and thereby aiding grain size reduction by nucleation of new grains.

Mineral reactions change the initial phase assemblage of Px+Pl to mostly Pl+Px+Zo in the synthetic mixtures, and Pl+Px+Amp +Qz+Zo in Maryland Diabase samples. Disregarding the differences in amount and type of mineral reactions, strain is always localized into a network of shear bands characterized by intense grain size reduction and phase mixing (to a lesser extent in the  
355 Ab+En sample; Figure 5).

The small size of grains in shear bands (Figure 11) clearly favours a grain size sensitive deformation mechanism such as DPC and grain boundary sliding. This interpretation is also supported by the strain free interior and grain morphology of the small grains in shear bands (Figure 9 and 10). The activity of solution-mass transport processes is clearly indicated by the vast extent of mineral reactions, which necessitate the movement of chemical components over several 10's of  $\mu\text{m}$  at least. The  
360 morphology of pores presented in Figure 9 is further supporting evidence for DPC interpretation; the pore trail in Figure 9d is interpreted to have formed by precipitation of plagioclase and entrapment of residual fluid along grain boundaries with a trace sub-parallel to the estimated  $\sigma_1$  direction (expected opening direction of dilatancy normal to  $\sigma_1$ ).

Concerning the albite CPO measured in the Ab+En sample, it is argued that the weak CPO is not due to dislocation creep, as discussed earlier. Rather, it is suggested that the CPO formed during grain size sensitive creep in the predominantly monomineralic albite layers. In the absence of further investigations it may be speculated that the CPO formation could be due to directed  
365 and anisotropic growth of the albite during DPC and grain boundary sliding of grains with a crystallographically controlled shape.

#### 4.6 Importance of dissolution-precipitation creep in natural rocks

Grain size reduction is energetically unfavourable as it increases the total grain surface area. DPC does not necessarily require  
370 the formation of new grains, instead, precipitation could take place as overgrowth rims on existing grains. The intense grain size reduction observed in shear bands within our experiments is most probably caused by high nucleation rates. High nucleation rates are typically attained by a large overstepping of a reaction boundary (e.g., Rubie, 1998; Putnis, 1992), introducing a high driving potential ( $\Delta G_t$ ). The start of our experiments represents such an instance of large overstepping of reaction boundaries. The starting materials +  $\text{H}_2\text{O}$  are not in equilibrium at the experimental Pc-T conditions. As the pressurization and heating  
375 procedure required to attain the experimental Pc-T conditions takes place within 5 – 8 h, the sample material is brought rapidly to a metastable state. Although this rapid change in P-T conditions is unique to experiments, there is widespread evidence from observations of natural rocks that similarly, metastable mineral assemblages can be sustained even at high-grade conditions



and to large overstepping of reaction boundaries, when rocks are dry (e.g., Rubie, 1986; Austrheim, 1987; Wayte et al., 1989; Krabbendam et al., 2000; Austrheim, 2013; Jamtveit et al., 2016). Only where fluid infiltrates, mineral reactions are enabled  
380 and equilibration can be attained.

TEM analyses revealed high defect densities in the albite porphyroclasts (Figure 9a, b). It has been proposed that a high intragranular defect density results in an increased rate of grain dissolution, speeding up the reaction and/or deformation rate (e.g., Wintsch, 1985; Schott et al., 1989; Stünitz, 1998). However, the observation of, e.g., abundant nucleation along former fractures (Figure 5k) cannot simply be accredited to enhanced reaction rates due to locally increased strain energy (in the sense  
385 of high defect densities locally introduced by fracturing according to, e.g., Fitz Gerald et al., 1991; Fitz Gerald and Stünitz, 1993; Stünitz et al., 2003; Trepmann et al., 2007). Fracturing is always accompanied by dilatancy. Fluid infiltrates the fractures, leading to higher solution-mass transport rates (e.g., Fitz Gerald and Stünitz, 1993; Precigout and Stünitz, 2016). Thus higher reaction rates can be expected. The significance of strain energy as a possible rate-enhancing contributor to reaction and nucleation is thus difficult to separate from the effects of enhanced fluid flow.

390 With the dominant deformation mechanisms, DPC and grain boundary sliding, the samples presented here deform viscously. At the experimentally induced conditions of  $T = 800\text{ °C}$  and at strain rates of  $\sim 3 \cdot 10^{-5}\text{ s}^{-1}$ , deformation takes place at the lower end of the viscous field, close to the brittle-viscous transition of the studied material (e.g., Marti et al., 2017). However, it is probable that the observed deformation mechanisms are also active at higher temperatures in these types of rocks. The principal constituent phases of mafic rocks (plagioclase + pyroxene + amphibole) all have high strengths in terms of intracrystalline  
395 plasticity, even at high temperatures. Where water is absent and DCP suppressed, the build-up of high stresses can be expected in such rocks, at least transiently (e.g., Okudaira et al., 2015). If local stresses are high enough to induce cracking, dilatancy and fluid infiltration may be facilitated. Once reactions start to operate (metastability of mafic rocks is very common because the mineral compositions are very variable and critically dependent on P, T, fluid-composition), a switch to DPC is likely to occur. The resulting deformation takes place with low stress exponents. It is clearly seen in our experiments that DPC and grain  
400 boundary sliding, as grain size sensitive deformation mechanisms, are strongly supported by the extensive mineral reactions causing grain size reduction by heterogeneous nucleation.

#### 4.7 Continued operation of deformation mechanisms at higher strain

In the case of the experimental set-up described here, where the starting mineral assemblages are not in equilibrium at the imposed P-T-fluid conditions, the chemical driving potential for attaining a lower energy assemblage partially controls the  
405 reaction rate. In principle, when the stable assemblage is reached, i.e., when the reaction has gone to completion, the driving potential for dissolution of phases is reduced, and it may be expected that the deformation rate is reduced, too. Interestingly, the measured amphibole compositions show variations, which are most probably influenced by the local mineral composition of the other phases in the neighbourhood (Figure 8). Shear offset and neighbour switching during deformation by diffusion creep and grain boundary sliding will continuously change the local neighbourhood of grains. As the neighbourhood of a  
410 given grain changes, so will new surfaces be exposed to the grain boundary fluid and become involved in reactions, potentially providing a relatively constant chemical driving force for reaction and nucleation, if local disequilibrium prevails. Thus, it may



take considerable time until the deforming assemblage has reached complete equilibrium, and some local chemical driving potentials may persist, even when the nominal bulk equilibrium assemblage has formed.

## 5 Summary and Conclusions

415 Viscous deformation in experiments with mafic compositions at temperatures of 800 °C and confining pressures of 1.0 and 1.5  
GPa at strain rates of  $\sim 10^{-5} \text{ s}^{-1}$  is dominantly achieved by dissolution-precipitation creep (DPC) and grain boundary sliding,  
accompanied by syn-deformational mineral reactions. No evidence for frictional deformation or significant contributions of  
dislocation glide or creep to the accommodation of strain can be found for any of the mineral phases. Strain is frequently lo-  
calised into shear bands, which consist of fine-grained mixtures of neo-crystallized plagioclase and the syn-kinematic reaction  
420 products amphibole, quartz and zoisite, none of which are present in the starting material.

Intense grain size reduction is produced by high nucleation rates, probably caused by a large overstepping of reaction bound-  
aries. Both, deformation and nucleation are localised in shear bands, implying a positive feedback between the two mecha-  
nisms.

Amphibole is seen to accommodate displacement via dissolution-precipitation creep, as interpreted from the evolution and  
425 distribution of amphibole coronas on pyroxene porphyroclasts. A weak but consistent crystallographic preferred orientation  
(CPO) of albite is formed in shear bands during deformation by DPC and grain boundary sliding.

The deformation in the samples takes place under conditions of pronounced weakening in all cases. The weakening is induced  
by strain localization into shear bands that show strong grain size reduction. Grain reduction, in turn, is due to nucleation of new  
phases, demonstrating the direct relationship between mineral reaction, grain size refinement, as well as the operation of DPC  
430 and grain boundary sliding (as grain size sensitive mechanisms), resulting in viscous deformation with low stress exponents.

*Code and data availability.* The MATLAB code for analysing amphibole reaction corona thicknesses is available from the author upon  
request ([sina.marti@ed.ac.uk](mailto:sina.marti@ed.ac.uk)). Mechanical data and chemical analyses are available from the author upon request.

## Appendix A: Methods

### A1 Sample preparation

435 Maryland Diabase rock powder is fabricated by crushing Maryland Diabase pieces with a hand-press and subsequently with an  
alumina hand-mortar. The resulting powder is dry-sieved to extract a grain size fraction  $\leq 125 \mu\text{m}$ . The plagioclase in Maryland  
Diabase shows a relatively homogeneous composition ( $\sim \text{An}_{65-70}$ ) except for a thin rim with lower anorthite component ( $\sim$   
 $\text{An}_{50-55}$ ). The core to rim area ratio is 83 : 17 ( $\pm 3$ ). Some of the clinopyroxene grains show a Mg-enriched core and  
clinopyroxene grains generally show orthopyroxene exsolution lamellae.

440 The diopside and enstatite material is a mineral powder provided by Jacques Precigout (University d'Orléans) and Holger



Stünitz (University of Tromsø, University d'Orléans) with grain sizes of 40 - 125  $\mu\text{m}$  for Cranberry Lake diopside, 40 - 180  $\mu\text{m}$  for Damaping enstatite. Damaping enstatite and diopside are derived from a peridotite xenolith, the Cranberry Lake diopside from a calc-silicate rock. The albite material is extracted from an albite-quartz vein formed along a joint from the Alpe Rischuna area, Switzerland. Sonora labradorite are labradorite megacrysts formed in basaltic deposits from the Pinacate  
445 volcanic field, Sonora, Mexico. From Sonora labradorite, Alpe Rischuna albite and Damaping diopside a powder (grain size fraction  $\leq 125 \mu\text{m}$ ) is produced in the same manner as described for the Maryland Diabase powder. As the Sonora labradorite material shows some accessory calcite, the powder is cleaned with  $\text{HCl}_{\text{aq}}$  (10%). Subsequently, the powder is placed in a funnel with a grade 602 h qualitative filter paper with a pore size of 2  $\mu\text{m}$  and rinsed thoroughly with distilled water. The powder retained by the filter is then dried in an oven at  $\sim 110 \text{ }^\circ\text{C}$ . After this treatment, no calcite is detected in the material.

450 Synthetic plagioclase-pyroxene powders are mixed with a phase distribution of  $\sim 57 \text{ vol}\%$  plagioclase to 43 vol% pyroxene. To produce the synthetic mixtures, the powders are placed in a 5 ml glass beaker with acetone and mixed using an ultrasonic stirrer (procedure of de Ronde et al., 2004). When most of the acetone is evaporated, the slurry is dried in an oven at 110  $^\circ\text{C}$ . This procedure prevents grain size and density sorting of the minerals.

The sample is then placed in a platinum jacket (0.15 mm wall thickness) with a 0.025 mm nickel foil insert. The Pt-jacket is  
455 weld-sealed with a Lampert welding apparatus while the sample is encased in a cooled brass piece ( $T \sim 4 \text{ }^\circ\text{C}$ ) to minimize sample heating and resulting potential water loss.

Solid sodium chloride ( $\text{NaCl}$ ) is used as confining medium (Appendix Figure A.1a). K-Type thermocouples (with metal tubing) positioned next to the sample are used for most experiments. Only for long-duration experiments of more than 6 days, S-type thermocouples (with mullite tubing) are used, as the mullite tubing is more durable in the corrosive environment of the heated  
460 salt.

## A2 Experimental procedure

Confining pressure, axial load, and displacement are constantly recorded. The force on the load-piston is measured using an external load cell, whereas the displacement of the load-piston is measured with either a direct current displacement transducer (resolution  $\sim 1 \mu\text{m}$ ) (Rig 1) or a noiseless digital linear-transformation measurement system (resolution = 0.1  $\mu\text{m}$ ) (Rig 2). Pc  
465 is measured via the oil pressure in the hydraulic pumping system and T is monitored and regulated to within  $\pm 1 \text{ }^\circ\text{C}$  via an Eurotherm controller.

To bring the sample to the desired Pc-T conditions during pressurisation, the independently movable Pc- and load-pistons are alternately advanced (thereby raising the pressure), accompanied by stepwise increases of temperature until the desired Pc-T conditions are reached (Appendix Figure A.1b). The pressurization procedure usually takes 5 – 8 h. During the actual deformation  
470 tion experiment, only the load-piston is advanced. The experimental setup necessitates that each deformation experiment starts with a so-called 'lead run-in', where the load-piston is advanced through a thin ( $\sim 1.5 \text{ mm}$ ) top lead layer. During this stage, the sample is expected to experience  $\sim$  isotropic pressure. During the initial lead run-in, the sample is under approximately hydrostatic conditions for several hours (usually between 24 - 30 h). Once the hit point is reached, sample loading initiates. At



the end of an experiment, the sample is quenched to 200 °C within 2 min while simultaneously removing the differential load.  
 475 Subsequently  $P_c$ , load and  $T$  are slowly and simultaneously reduced to room conditions within about 5 h.

### A3 Evaluation of mechanical data

Axial displacement is corrected for apparatus stiffness.  $\sigma_3$  is assumed to be equal to the confining pressure,  $P_c$  (Eq. (A1)). With increasing advancement of the load-piston, the pressure inside the vessel increases and  $P_c$  is corrected for this (see e.g., Richter et al., 2016). The differential stress,  $\Delta\sigma$ , acting on the sample is derived from the difference between the axial load ( $F$ ) with  
 480 reference to the load at the hit point ( $F_0$ ) (Eq. (A2)), and the cross-sectional area of the forcing block (31.47 mm<sup>2</sup>)

$$\sigma_3 = P_c \quad (\text{A1})$$

$$\Delta\sigma = (F - F_0)/31.47\text{mm}^2 \quad (\text{A2})$$

$\Delta\sigma$  in the sample is corrected for the decreasing overlap of the forcing blocks (see procedure described in Marti et al., 2017). The shear and normal stresses,  $\tau$  and  $\sigma_n$  supported by the sample inclined at 45° are obtained by Mohr circle construction from  
 485  $\Delta\sigma$ . The effective pore fluid pressures in our experiments is assumed to be negligible, i.e. is taken as zero and the deviation of  $\sigma_1$  by 3-6° from 45° is neglected as well.

Stress exponent,  $n$ , is calculated for a relationship

$$\tau = \dot{\gamma}_a^{1/n} \quad (\text{A3})$$

between shear stress,  $\tau$ , and strain rate,  $\dot{\gamma}_a$ , (Eq. (A3)) using data of displacement-rate stepping and single-displacement rate  
 490 experiments.

Over the years and between the different laboratories, different data treatment routines have been developed and are in use. The variations in calculated stresses using the different methods can influence determined stress exponents ( $n$ ) from the data, causing variations on the order of 16 – 27 % on determined  $n$  values (see Marti et al., 2017)

### A4 Strain and flow descriptors

495 The ISA and the finite stretching direction can be derived because the initial thickness of the shear zone is known (with an error of  $\pm 0.03$  mm) and the end-thickness can be measured after the experiment from the thin section. This uncertainty associated with the initial thickness leads to some uncertainty concerning the amount of thinning, and therefore also to a range of values for the ISA, the finite stretching direction and  $W_k$ .

### A5 Microstructure analysis

500 - *Data acquisition*

SEM analyses are performed either with the Zeiss Merlin SEM at Tromsø University, or with a Philips XL30 ESEM at the



Nano Imaging Lab of the Swiss Nanoscience Institute (SNI) at Basel University. Chemical analyses are performed using standardless energy dispersive X-ray Spectrometry (EDS), at 15 keV acceleration voltage with a ZAF matrix correction for spectra quantification.

505 (Scanning) transmission electron microscopy ((S)TEM) analyses are performed at Utrecht University using a FEI Talos 200FX equipped with a high-sensitivity Super-EDX system. TEM images are recorded in bright field (BF) mode, whereas STEM images in high angular annular dark field (HAADF) mode. BF-TEM images are highly sensitive on crystallographic orientation, whereas contrasts in HAADF-STEM images are sensitive to average atomic number (Z-contrast) of the material. Focussed ion beam (FIB) foils for TEM investigations are prepared using an FEI Helios NanoLab G3. The FIB foils are cut parallel to  
510 the shear direction and normal to the shear plane. Both, the FEI Talos 200FX and the Nanolab 3G are located at the Electron microscopy square at Utrecht University.

#### - EBSD analysis

For Electron backscatter diffraction (EBSD) measurements, thin sections were polished with colloidal silica suspension and  
515 subsequently coated with a thin layer of carbon. Samples were analysed in the Zeiss Merlin SEM at the University of Tromsø, with a Nordlys nano camera in high vacuum at 15 keV acceleration voltage and probe currents of  $\sim 15$  nA. Data is acquired with the Oxford AZtec software and processed with Channel 5 and the MATLAB toolbox MTEX (available at <https://mtex-toolbox.github.io>; Bachmann et al., 2010). Pole figures are plotted using MTEX. For pole figure contouring, the de la Vallée Poussin kernel with a half-width of  $9.4^\circ$  and a bandwidth of 30 is used. Pole figure J-index (PFJ; e.g., Bunge, 1982; Mainprice  
520 and Silver, 1993) are given as a measure of texture strength. The index has a value of 1 for a random distribution and is infinite for a single orientation.

#### - Image analysis

Phase segmentation: Phase segmentation is performed on BSE SEM images, where individual minerals are identified by their Z-  
525 contrast. Using the software Fiji (link at: <http://fiji.sc/Fiji>) and the plugin Statistical Region Merger, automatic pre-segmentation was achieved. The automatic segmentation was then manually inspected and corrected where necessary.

Grain maps: Grain maps were produced by manually tracing (supervised segmentation) grains from SEM or TEM images. Grains were analyzed for their 2D area using Fiji, and for each grain, the diameter of the area equivalent circle,  $d_{equ}$ , is  
530 calculated.

$$d_{equ} = 2 \cdot \sqrt{(A/\pi)} \quad (A4)$$

where A is the area of the digitized shape. Grain size distributions are presented as histograms of the 2D number weighted distribution of equivalent diameters.

Shear band orientation: Shear bands are traced and digitized on BSE SEM images. The x-y-coordinates of the outlines of the  
535 digitized structures are smoothed to remove pixel artefacts, and exported using Fiji. The smoothed x-y-coordinates are used as



input for the SURFOR program (Panozzo Heilbronner, 1984; Heilbronner and Barrett, 2014), which determines the orientation distribution function (ODF) of the boundary segments. The ODFs are presented as rose diagrams.

*Acknowledgements.* We thank the team of the centre of nano imaging (SNI) at Basel University and Tom Eilertsen at Tromso University for help and assistance with the electron microscopy. Terry Tullis is thanked for providing the Maryland Diabase material and the Cranberry Lake Diopside was kindly provided by Jacques Précigout. Willy Tschudin is thanked for excellent thin section preparation. We gratefully acknowledge the funding provided by the Swiss National Foundation grant NF 200020\_144448 and financial support from the Freiwillige Akademische Gesellschaft, Basel, during the last stages of finishing this manuscript.



## References

- Ashby, M. F. and Verrall, R. A.: Diffusion-accommodated Flow and Superplasticity, *Acta Metallurgica*, 21, 149 – 163, 1973.
- 545 Austrheim, H.: Eclogitization of lower crustal granulites by fluid migration through shear zones, *Earth and Planetary Science Letters*, 81, 221 – 232, 1987.
- Austrheim, H.: Fluid and deformation induced metamorphic processes around Moho beneath continent collision zones: Examples from the exposed root zone of the Caledonian mountain belt, W-Norway, *Tectonophysics*, 609, 620 – 635, 2013.
- Bachmann, F., Hielscher, R., and Schaeben, H.: Texture Analysis with MTEX - Free and Open Source Software Toolbox, *Solid State*  
550 *Phenomena*, 160, 63 – 68, 2010.
- Barreiro, J. G., Lonardelli, I., Wenk, H., Dresen, G., Rybacki, E., Ren, Y., and Tome, C.: Preferred orientation of anorthite deformed experimentally in Newtonian creep, *Earth and Planetary Science Letters*, 264, 188 – 207, 2007.
- Berger, A. and Herwegh, M.: Grain coarsening in contact metamorphic carbonates: effects of second-phase particles, fluid flow and thermal perturbations, *Journal of Metamorphic Geology*, 22, 459 – 474, 2004.
- 555 Berger, A. and Stünitz, H.: Deformation mechanisms and reaction of hornblende: examples from the Bergell tonalite (Central Alps), *Tectonophysics*, 257, 149 – 174, 1996.
- Bons, P. D. and den Brok, B.: Crystallographic preferred orientation development by dissolution-precipitation creep, *Journal of Structural Geology*, 22, 1713 – 1722, 2000.
- Brander, L., Svahnberg, H., and Piazzolo, S.: Brittle-plastic deformation in initially dry rocks at fluid-present conditions: transient behaviour  
560 of feldspar at mid-crustal levels, *Contribution to Mineralogy and Petrology*, 163, 403 – 425, 2012.
- Brodie, K. H. and Rutter, E. H.: The role of transiently fine-grained reaction products in syntectonic metamorphism: natural and experimental examples, *Canadian Journal of Earth Sciences*, 24, 556 – 564, 1987.
- Bunge, H. J.: *Texture Analysis in Materials Sciences*, Butterworth, London, 1982.
- Bürgmann, R. and Dresen, G.: Rheology of the Lower Crust and Upper Mantle: Evidence from Rock Mechanics, Geodesy, and Field  
565 Observations, *Annu. Rev. Earth Planet. Sci.*, 36, 531 – 567, 2008.
- Burov, E. B.: Rheology and strength of the lithosphere, *Marine and Petroleum Geology*, 28, 1402 – 1443, 2011.
- Bystricky, M. and Mackwell, S.: Creep of dry clinopyroxene aggregates, *Journal of Geophysical Research*, 106, 13 443 – 13 454, 2001.
- Chen, S., Hiraga, T., and Kohlstedt, D. L.: Water weakening of clinopyroxene in the dislocation creep regime, *Journal of Geophysical Research*, 111, B08 203, 2006.
- 570 Coble, R. L.: A Model for Boundary Diffusion Controlled Creep in Polycrystalline Materials, *Journal of Applied Physics*, 34, 1679 – 1682, 1963.
- de Ronde, A. A., Heilbronner, R., Stünitz, H., and Tullis, J.: Spatial correlation of deformation and mineral reaction in experimentally deformed plagioclase-olivine aggregates, *Tectonophysics*, 389, 93–109, 2004.
- de Ronde, A. A., Stünitz, H., Tullis, J., and Heilbronner, R.: Reaction-induced weakening of plagioclase-olivine composites, *Tectonophysics*,  
575 409, 85 – 106, 2005.
- Derby, B.: The dependence of grain size on stress during dynamic recrystallisation, *Acta Metall. Mater.*, 39, 955 – 962, 1991.
- Dimanov, A. and Dresen, G.: Rheology of synthetic anorthite-diopside aggregates: Implications for ductile shear zones, *Journal of Geophysical Research*, 110, B07 203, 2005.



- Dimanov, A., Dresen, G., Xiao, X., and Wirth, R.: Grain boundary diffusion creep of synthetic anorthite aggregates: The effect of water,  
580 Journal of Geophysical Research, 104, 10 483 – 10 497, 1999.
- Dimanov, A., Lavie, M. P., Dresen, G., Ingrin, J., and Jaoul, O.: Creep of polycrystalline anorthite and diopside, Journal of Geophysical  
Research, 108, B001 815, 2003.
- Dimanov, A. E., Rybacki, E., Wirth, R., and Dresen, G.: Creep and strain-dependent microstructures of synthetic anorthite-diopside aggre-  
gates, Journal of Structural Geology, 29, 1049 – 1069, 2007.
- 585 Drury, M., Avé Lallemant, H., Pennock, G., and Palasse, L.: Crystal preferred orientation in peridotite ultramylonites deformed by grain size  
sensitive creep, Étang de Lers, Pyrenees, France, Journal of Structural Geology, 33, 1776–1789, 2011.
- Etheridge, M. A. and Wilkie, J. C.: Grain size reduction, grain boundary sliding and the flow strength of mylonites, Tectonophysics, 58, 159  
– 178, 1979.
- Fitz Gerald, J. D. and Stünitz, H.: Deformation of Granitoids at low Metamorphic Grade. 1. Reactions and Grain-size Reduction, Tectono-  
590 physics, 221, 269 – 297, 1993.
- Fitz Gerald, J. D., Boland, J. N., McLaren, A. C., Ord, A., and Hobbs, B.: Microstructures in water-weakened single crystals of quartz,  
Journal of Geophysical Research - Solid Earth, 96, 2139 – 2155, 1991.
- Fossen, H. and Tikoff, B.: The deformation matrix for simultaneous simple shearing, pure shearing and volume change, and its application  
to transpression-transension tectonics, Journal of Structural Geology, 15, 413 – 422, 1993.
- 595 Fukuda, J.-I. and Okudaira, T.: Grain-size-sensitive Creep of Plagioclase accompanied by Solution-Precipitation and Mass Transfer under  
Mid-crustal Conditions, Journal of Structural Geology, 51, 61 – 73, 2013.
- Getsinger, A. J. and Hirth, G.: Amphibole fabric formation during diffusion creep and the rheology of shear zones, Geology, 42, 535 – 538,  
2014.
- Gratier, J.-P., Guiget, R., Renard, F., Jenatton, L., and Bernard, D.: A pressure solution creep law for quartz from indentation experiments,  
600 Journal of Geophysical Research, 114, B03 403, 2009.
- Gratier, J.-P., Dysthe, D. K., and Francois, R.: The role of pressure solution creep in the ductility of the Earth's upper crust, vol. 54 of  
*Advances in Geophysics*, pp. 47 – 179, 2013.
- Hawthorne, F., Oberti, R., Harlow, G., Maresch, W., Martin, R., Schumacher, J., and Welch, M.: Nomenclature of the amphibole supergroup,  
American Mineralogist, 97, 2031 – 2048, 2012.
- 605 Heilbronner, R. and Barrett, S.: Image Analysis in Earth Sciences - Microstructures and Textures of Earth Materials, Springer-Verlag, Berlin,  
2014.
- Hickman, S. H. and Evans, B.: Experimental pressure solution in halite: the effect of grain/interphase boundary structure, Journal of the  
Geological Society, London, 148, 549 – 560, 1991.
- Hier-Majumder, S., Mei, S., and Kohlstedt, D. L.: Water weakening of clinopyroxenite in diffusin creep, Journal of Geophysical Research,  
610 110, B07 406, 2005.
- Imon, R., Okudaira, T., and Fujimoto, A.: Dissolution and precipitation processes in deformed amphibolites: an example from the ductile  
shear zone of the Ryoke metamorphic belt, SW Japan, Journal of metamorphic Geology, 20, 297 – 308, 2002.
- Jamtveit, B., Austrheim, H., and Putnis, A.: Disequilibrium metamorphism of stressed lithosphere, Earth-Science Reviews, 154, 1 – 13, 2016.
- Ji, S., Jiang, Z., Rybacki, E., Wirth, R., Prior, D. J., and Xia, B.: Strain softening and microstructural evolution of anorthite aggregates and  
615 quartz-anorthite layered composites deformed in torsion, Earth and Planetary Science Letters, 222, 377 – 390, 2004.



- Jiang, Z., Prior, D. J., and Wheeler, J.: Albite crystallographic preferred orientation and grain misorientation distribution in a low-grade mylonite: implications for granular flow, *Journal of Structural Geology*, 22, 1663 – 1674, 2000.
- Karato, S.-I.: *Deformation of Earth Materials - an introduction to the rheology of solid earth*, Cambridge University Press, Cambridge, 2008.
- Kilian, R., Heilbronner, R., and Stünitz, H.: Quartz grain size reduction in a granitoid rock and the transition from dislocation to diffusion creep, *Journal of Structural Geology*, 33, 1265 – 1284, 2011.
- 620 Kohlstedt, D. L. and Hansen, L. N.: Constitutive equations, rheological behavior, and viscosity of rocks, in: *Treatise on Geophysics*, edited by Schubert, G., pp. 441 – 472, Elsevier, 2015.
- Kohlstedt, D. L., Evans, B., and Mackwell, S. J.: Strength of the Lithosphere: Constraints imposed by laboratory experiments, *Journal of Geophysical Research - Solid Earth*, 100, 517 – 587, <https://doi.org/10.1029/95JB01460>, 1995.
- 625 Kollé, J. J. and Blacic, J. D.: Deformation of Single-Crystal Clinopyroxenes: Mechanical Twinning in Diopside and Hedenbergite, *Journal of Geophysical Research*, 87, 4019 – 4034, 1982.
- Krabbendam, M., Wain, A., and Andersen, T. B.: Pre-Caledonian granulite and gabbro enclaves in the Western Gneiss Region, Norway: indications of incomplete transition at high pressure, *Geological Magazine*, 137, 235 – 255, 2000.
- Kronenberg, A. K. and Shelton, G. L.: Deformation microstructures in experimentally deformed Maryland Diabase, *Journal of Structural Geology*, 2, 341 – 353, 1980.
- 630 Kruse, R., Stünitz, H., and Kunze, K.: Dynamic recrystallization processes in plagioclase porphyroclasts, *Journal of Structural Geology*, 23, 1781 – 1802, 2001.
- Lallemant, H. A.: Experimental Deformation of Diopside and Websterite, *Tectonophysics*, 48, 1 – 27, 1978.
- Lapworth, T., Wheeler, J., and Prior, D. J.: The Deformation of Plagioclase investigated using Electron Backscatter Diffraction Crystallographic Preferred Orientation Data, *Journal of Structural Geology*, 24, 387 – 399, 2002.
- 635 Linckens, J., Herwegh, M., Müntener, O., and Mercolli, I.: Evolution of a polymineralic mantle shear zone and the role of second phases in the localization of deformation, *Journal of Geophysical Research*, 116, B06 210, 2011.
- Mainprice, D. and Silver, P. G.: Interpretation of SKS-waves using samples from the subcontinental lithosphere, *Physics of the Earth and Planetary Interiors*, 78, 257 – 280, 1993.
- 640 Marsh, J., Johnson, S., Yates, M., and West, J.: Coupling of deformation and reactions during mid-crustal shear zone development: an in situ frictional-viscous transition., *Journal of metamorphic Geology*, 27, 531–553, 2009.
- Marti, S., Stünitz, H., Heilbronner, R., Plümper, O., and Drury, M.: Experimental investigation of the brittle-viscous transition in mafic rocks – Interplay between fracturing, reaction, and viscous deformation, *Journal of Structural Geology*, 105, 62 – 79, 2017.
- Mauler, A., Bystricky, M., Kunze, K., and Mackwell, S.: Microstructures and lattice preferred orientations in experimentally deformed clinopyroxene aggregates, *Journal of Structural Geology*, 22, 1633 – 1648, 2000.
- 645 Mehl, L. and Hirth, G.: Plagioclase preferred orientation in layered mylonites: Evaluation of flow laws for the lower crust, *Journal of Geophysical Research - Solid Earth*, 113, B05 202, 2008.
- Mukai, H., Austrheim, H., Putnis, C. V., and Putnis, A.: Textural Evolution of Plagioclase Feldspar across a Shear Zone: Implications for Deformation Mechanism and Rock Strength, *Journal of Petrology*, 55, 1457 – 1477, 2014.
- 650 Newman, J., Lamb, W. M., Drury, M. R., and Vissers, R. L. M.: Deformation processes in a peridotite shear zone: reaction-softening by an H<sub>2</sub>O-deficient, continuous net transfer reaction, *Tectonophysics*, 303, 193 – 222, 1999.



- Okudaira, T., Jerabek, P., H., S., and Füsseis, F.: High-temperature fracturing and subsequent grain-size-sensitive creep in lower crustal gabbros: Evidence for coseismic loading followed by creep during decaying stress in the lower crust?, *Journal of Geophysical Research - Solid Earth*, 120, 3119 – 3141, 2015.
- 655 Olgaard, D. L. and Evans, B.: Effect of Second-Phase Particles on Grain Growth in Calcite, *Journal of the American Ceramic Society*, 69, 272 – 277, 1986.
- Panozzo Heilbronner, R.: Two-dimensional strain from the orientation of lines in a plane, *Journal of Structural Geology*, 6, 215 – 221, 1984.
- Paterson, M. S.: *Materials Science for Structural Geology*, Springer, Dordrecht, 2013.
- Precigout, J. and Stünitz, H.: Evidence of phase nucleation during olivine diffusion creep: A new perspective for mantle strain localisation, 660 *Earth and Planetary Science Letters*, 455, 94–105, 2016.
- Putnis, A.: *Introduction to mineral sciences*, Cambridge University Press, New York, 1992.
- Raterron, P. and Jaoul, O.: High-temperature deformation of diopside single crystal, 1. mechanical data, *Journal of Geophysical Research*, 96, 14 277 – 14 286, 1991.
- Richter, B., Stünitz, H., and Heilbronner, R.: Stresses and pressures at the quartz-to-coesite phase transformation in shear- deformation 665 experiments, *Journal of Geophysical Research - Solid Earth*, 121, JB013 084, 2016.
- Rosenberg, C. L. and Stünitz, H.: Deformation and recrystallization of plagioclase along a temperature gradient: an example from the Bergell tonalite, *Journal of Structural Geology*, 25, 389 – 408, 2003.
- Rubie, D. C.: The catalysis of mineral reaction by water and restrictions of the presence of aqueous fluid during metamorphism, *Mineralogical Magazine*, 50, 399 – 415, 1986.
- 670 Rubie, D. C.: Disequilibrium during metamorphism: the role of nucleation kinetics, *Geological Society Special Publication*, 138, 199 – 214, 1998.
- Rutter, E. H., Peach, C. J., White, S. H., and Johnston, D.: Experimental 'syntectonic' hydration of basalt, *Journal of Structural Geology*, 7, 251 – 266, 1985.
- Rybacki, E. and Dresen, G.: Dislocation and diffusion creep of synthetic anorthite aggregates, *Journal of Geophysical Research - Solid 675 Earth*, 105, 26 017 – 26 036, 2000.
- Schmid, E. and Boas, W.: *Plasticity of Crystals with Special Reference to Metals*, F.A. Hughes, London, 1950.
- Schott, J., Brantley, S., Crerar, D., Guy, C., Borcsik, M., and Willaime, C.: Dissolution kinetics of strained calcite, *Geochemica et Cosmochimica Acta*, 53, 373 – 382, 1989.
- Shaocheng, J. and Bin, X.: *Rheology of polyphase earth materials*, Polytechnic International Press, Montreal, 2002.
- 680 Shaocheng, J. and Mainprice, D.: Experimental deformation of sintered albite above and below the ordered-disorder transition, *Geodinamica Acta (Paris)*, 1, 113 – 124, 1987.
- Shelley, E.: Spider texture and amphibole preferred orientations, *Journal of Structural Geology*, 16, 709–717, 1994.
- Shigmeatsu, N. and Tanaka, H.: Dislocation creep of fine-grained recrystallized plagioclase under low-temperature conditions, *Journal of Structural Geology*, 22, 65 – 79, 2000.
- 685 Stokes, M., Wirth, R., and Southworth, C.: Deformation of amphibolites via dissolution-precipitation creep in the middle and lower crust, *Journal of metamorphic Geology*, 30, 723 – 737, 2012.
- Stünitz, H.: Syndeformational recrystallization - dynamic or compositionally induced?, *Contributions to Mineralogy and Petrology*, 131, 219 – 236, 1998.



- 690 Stünitz, H. and Tullis, J.: Weakening and strain localization produced by syn-deformational reaction of plagioclase, *International Journal of Earth Sciences*, 90, 136 – 148, 2001.
- Stünitz, H., Fitz Gerald, J. D., and Tullis, J.: Dislocation generation, slip systems, and dynamic recrystallization in experimentally deformed plagioclase single crystals, *Tectonophysics*, 372, 215 – 233, 2003.
- Sundberg, M. and Cooper, R. F.: Crystallographic preferred orientation produced by diffusional creep of harzburgite: Effects of chemical interactions among phases during plastic flow, *Journal of Geophysical Research*, 113, B12 208, 2008.
- 695 Tikoff, B.: The limitations of three-dimensional kinematic vorticity analysis, *Journal of Structural Geology*, 17, 1771 – 1784, 1995.
- Trepmann, C. A., Stöckert, B., Dorner, D., Moghadam, R. H., Küster, M., and Röller, K.: Simulating coseismic deformation of quartz in the middle crust and fabric evolution during postseismic stress relaxation - An experimental study, *Tectonophysics*, 442, 83 – 104, 2007.
- Tullis, J. and Yund, A.: Dynamic recrystallization of feldspar: A mechanism for ductile shear zone formation, *Geology*, 13, 238 – 241, 1985.
- Tullis, J. and Yund, A.: Diffusion creep in feldspar aggregates: experimental evidence, *Journal of Structural Geology*, 13, 987 – 1000, 1991.
- 700 Viegas, G., Menegon, L., and Archanjo, C.: Brittle grain-size reduction of feldspar, phase mixing and strain localization in granitoids at mid-crustal conditions (Pernambuco shear zone, NE Brazil), *Solid Earth*, 7, 375 – 396, 2016.
- Wayte, G. J., Worden, R. H., Rubie, D. C., and Droop, G. T. R.: A TEM study of disequilibrium plagioclase breakdown at high pressure: the role of infiltrating fluid, *Contribution to Mineralogy and Petrology*, 101, 426 – 437, 1989.
- Wheeler, J.: Importance of Pressure Solution and Coble Creep in the Deformation of Polymineralic Rocks, *Journal of Geophysical Research*, 705 97, 4579 – 4586, 1992.
- Whitney, D. and Evans, B. W.: Abbreviations for names of rock-forming minerals, *American Mineralogist*, 95, 185 – 187, 2010.
- Wintsch, R. P.: *The Possible Effects of Deformation on Chemical Processes in Metamorphic Fault Zones*, *Advances in Physical Geochemistry*, 4, Springer-Verlag, N.Y., 1985.
- Xie, Y., Wenk, H.-R., and Matthies, S.: Plagioclase preferred orientation by TOF neutron diffraction and SEM-EBSD, *Tectonophysics*, 370, 710 269 – 286, 2003.
- Yund, R. A. and Tullis, J.: Compositional change of minerals associated with dynamic recrystallization, *Contributions to Mineralogy and Petrology*, 108, 346 – 355, 1991.
- Zhang, J., Green, H. W., and Bozhilov, K. N.: Rheology of omphacite at high temperature and pressure and significance of its lattice preferred orientations, *Earth and Planetary Science Letters*, 246, 432 – 443, 2006.

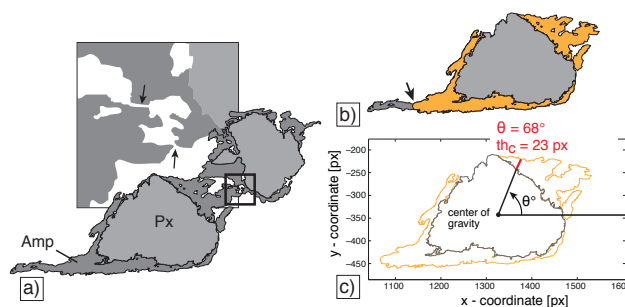


**Figure 1.** Analysis of amphibole corona thickness. a) Digital phase map of segmented Pyroxene (Px) clasts and associated amphibole (Amp) coronas. Where adjacent coronas are in contact, they are separated manually (close-up, black arrows). b) Long ‘tails’ of Amp growing in low stress sites around clasts are eventually ‘cut’ (black arrow) if they are extending too far away from the clast. c) Corona thickness,  $th_c(\theta)$ , is determined from the polar coordinates of the aggregate and clast outline as a function of the angle  $\theta$  ( $0^\circ < \theta < 360^\circ$ ), with  $\theta$  running CCL from the horizontal.



**Table 1.** Mineral composition. Representative mineral measurements as normalised oxide wt% and as calculated stoichiometric mineral composition for the different starting materials. All Fe is taken as Fe<sup>2+</sup> due to the reducing environment in the sample assembly.

wt.-%	Alpe Rischuna	Sonora	Maryland Diabase		wt.-%	Cranberry	Damaping	Damaping	Maryland	Maryland
	Albite	Labradorite	Plagioclase core rim			lake Diopside	Diopside	Enstatite	Diabase Cpx	Diabase Opx
SiO <sub>2</sub>	67.87	53.66	51.86	55.67	SiO <sub>2</sub>	57.18	54.39	55.98	51.58	52.61
Al <sub>2</sub> O <sub>3</sub>	20.14	30.37	29.92	27.72	Al <sub>2</sub> O <sub>3</sub>	0.85	6.37	4.01	1.77	0.75
CaO	0.21	11.09	13.39	10.57	CaO	22.54	17.93	0.80	14.71	1.44
Na <sub>2</sub> O	11.71	3.90	3.63	5.11	Na <sub>2</sub> O	0.39	1.71	0.27	0.28	0.00
K <sub>2</sub> O	0.10	0.39	0.26	0.37	K <sub>2</sub> O	0.00	0.00	0.00	0.00	0.00
MgO	0.00	0.00	0.00	0.00	MgO	17.93	16.13	33.28	14.03	19.36
TiO <sub>2</sub>	0.00	0.00	0.00	0.00	TiO <sub>2</sub>	0.00	0.34	0.00	0.76	0.28
FeO	0.00	0.59	0.94	0.55	FeO	1.11	2.37	5.13	16.40	25.55
MnO	0.00	0.00	0.00	0.00	MnO	0.00	0.00	0.00	0.48	0.00
Cr <sub>2</sub> O <sub>3</sub>	0.00	0.00	0.00	0.00	Cr <sub>2</sub> O <sub>3</sub>	0.00	0.76	0.53	0.00	0.00
<b>Total:</b>	<b>100.00</b>	<b>100.00</b>	<b>100.00</b>	<b>99.99</b>	<b>Total:</b>	<b>100.00</b>	<b>100.00</b>	<b>100.00</b>	<b>100.01</b>	<b>99.99</b>
<b>Atoms per 8 oxygen</b>					<b>Atoms per 6 oxygen</b>					
Si	2.97	2.42	2.36	2.51	Si	2.04	1.94	1.92	1.95	1.99
Al	1.04	1.61	1.61	1.47	Al	0.04	0.27	0.16	0.08	0.03
Ca	0.01	0.54	0.65	0.51	Ca	0.86	0.68	0.03	0.60	0.06
Na	0.99	0.34	0.32	0.45	Na	0.03	0.12	0.02	0.02	0.00
K	0.01	0.02	0.02	0.02	K	0.00	0.00	0.00	0.00	0.00
Mg	0.00	0.00	0.00	0.00	Mg	0.95	0.86	1.70	0.79	1.09
Ti	0.00	0.00	0.00	0.00	Ti	0.00	0.01	0.00	0.02	0.01
Fe	0.00	0.02	0.04	0.02	Fe	0.03	0.07	0.15	0.52	0.81
<b>Mn</b>	<b>0.00</b>	<b>0.00</b>	<b>0.00</b>	<b>0.00</b>	<b>Mn</b>	<b>0.00</b>	<b>0.00</b>	<b>0.00</b>	<b>0.02</b>	<b>0.00</b>
<b>Cr</b>	<b>0.00</b>	<b>0.00</b>	<b>0.00</b>	<b>0.00</b>	<b>Cr</b>	<b>0.00</b>	<b>0.02</b>	<b>0.01</b>	<b>0.00</b>	<b>0.00</b>
<b>Total</b>	<b>5.01</b>	<b>4.96</b>	<b>5.00</b>	<b>4.97</b>	<b>Total</b>	<b>3.95</b>	<b>3.97</b>	<b>4.00</b>	<b>4.00</b>	<b>3.99</b>
An	0.98	0.60	0.66	0.52	En	0.52	0.53	0.91	0.42	0.56
Ab	98.47	0.38	0.32	0.46	Fe	0.02	0.04	0.08	0.27	0.41
Or	0.55	0.02	0.02	0.02	Wo	0.47	0.42	0.02	0.31	0.03



**Table 2.** Experimental conditions.

Exp. nr.	Material	Pc [GPa]	peak $\tau$ [MPa]	$\tau$ at end [MPa]	mean $\dot{\gamma}_a$ [s <sup>-1</sup> ]	$\mu$ l H <sub>2</sub> O added	$\gamma_a$	th0 [mm]	thF [mm]	ds [mm]	$\gamma$	k	wk	shortening ISA [°]	$\Psi$ [°]	R
414	MD	0.97	407	192	2.1e-5 <sup>1</sup>	0.20	5.12	0.75	0.50	2.56	3.32	1.50	0.972	38.1	9.3	14.3
449	MD	1.50	479	337	2.3e-5 <sup>1</sup>	0.20	4.51	0.75	0.61	2.75	3.64	1.23	0.994	41.8	11.3	15.6
468*	MD	1.07	348		1.2e-5 <sup>3</sup>	0.20	0.70	0.75	0.69	0.48	0.64	1.09	0.968	37.7	28.8	1.9
470*	MD	1.50	446		1.3e-5 <sup>3</sup>	0.20	0.86	0.75	0.69	0.65	0.86	1.09	0.982	39.5	27.9	2.3
484**	MD	1.02	371	316 233	1.9e-5 <sup>2</sup> 9.5e-6 <sup>2</sup>	0.20	1.97	0.75	0.56	1.33						
489	MD	1.05	428	286	1.9e-5 <sup>1</sup>	0.20	3.04	0.75	0.63	1.91	2.54	1.19	0.991	41.1	15.3	8.5
490**	MD	1.00	350		2.4e-5 <sup>2</sup> 1.2e-5 <sup>2</sup> 2.5e-6 <sup>2</sup>	0.20	5.37	0.75	0.53	2.84	3.72	1.42	0.983	39.7	9.3	16.8
491**	MD	1.52	388		1.7e-5 <sup>2</sup> 8.0e-6 <sup>2</sup> 2.3e-6 <sup>2</sup>	0.20	4.97	0.75	0.54	2.68	3.52	1.39	0.983	39.7	10.0	15.2
492	MD	1.01	468	197	2.6e-5 <sup>1</sup>	0.20	8.95	0.75	0.44	3.94	5.01	1.70	0.978	39.0	5.8	30.8
502**	MD	1.52	391		1.8e-5 <sup>2</sup> 8.1e-6 <sup>2</sup> 1.7e-6 <sup>2</sup>	0.20	3.90	0.75	0.58	2.26	2.98	1.29	0.985	40.1	12.3	11.3
503	An60+En	1.03	530	367	2.6e-5 <sup>1</sup>	0.12	6.55	0.75	0.55	3.60	4.73	1.36	0.992	41.3	8.1	25.4
505	An60+Di (CLk)	1.01	460	253	2.5e-5 <sup>1</sup>	0.12	6.17	0.75	0.55	3.39	4.45	1.36	0.990	41.0	8.5	22.8
507	MD	1.04	479	191	2.4e-5 <sup>1</sup>	0.12	5.82	0.75	0.49	2.85	3.69	1.53	0.974	38.5	8.4	17.2
518	Ab+En	1.02	511	263	2.4e-5 <sup>1</sup>	0.12	5.83	0.75	0.54	3.15	4.12	1.39	0.988	40.5	8.8	20.0
519	En60+Di (D)	1.02	517	289	2.2e-5 <sup>1</sup>	0.12	5.60	0.75	0.54	3.02	3.96	1.39	0.987	40.3	9.1	18.6

MD=Maryland Diabase, Slab=Sonora Labradorite, En=Damaping Enstatite, Di (CLk)=Cranberry lake Diopside, Di(D)=Damaping Diopside, Ab=Alpe Rischuna Albite. \* experiment terminated at peak-stress. \*\* displacement-rate stepping test.  $\Psi$  = finite stretching direction, R = ratio strain ellipse major vs minor axis.

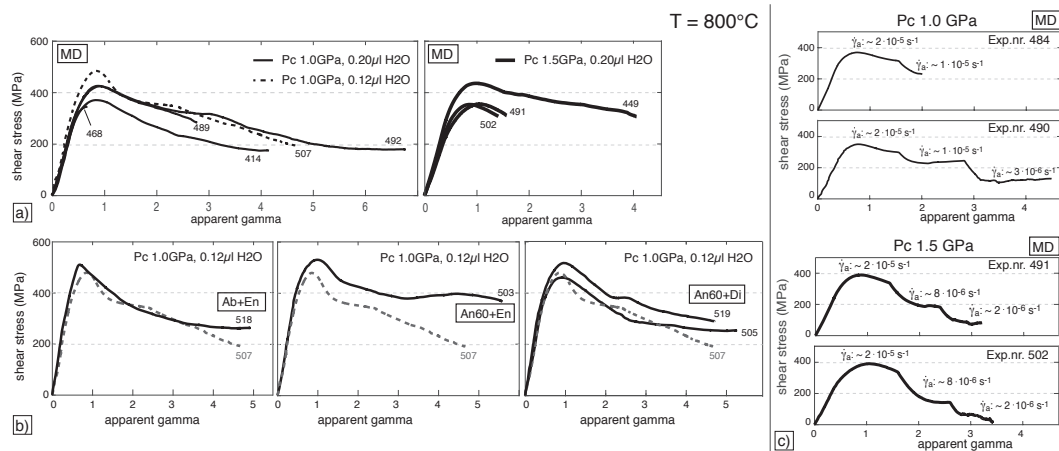


**Figure 2.** Mechanical data. Shear stress,  $\tau$  (MPa), versus apparent shear strain,  $\gamma_a$ . Stippled line = Experiment 507 (MD) for reference. a) Maryland Diabase (MD) experiments for different confining pressures,  $P_c$  (GPa), and water contents. b) Experiments using different PI-Px mixtures and constant  $P_c$  and water content. c) Displacement-rate stepping tests on MD sample material for experiments performed at different confining pressures.

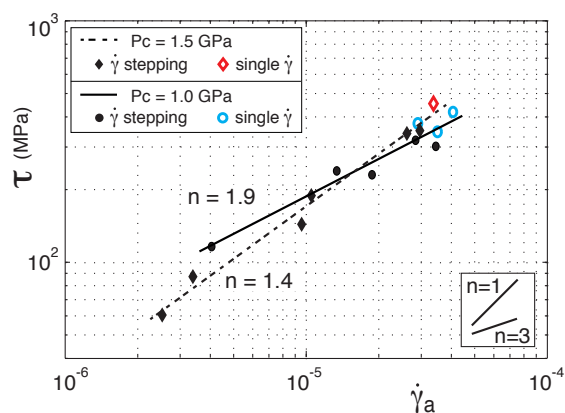


**Figure 3.** Determination of stress exponents. Shear stress,  $\tau$  (MPa), versus apparent shear strain rate,  $\dot{\gamma}_a$ . Two stress exponents,  $n$ , are obtained using constant strain rate data and strain rate stepping experiments. For experiments at confining pressures,  $P_c = 1.0$  GPa,  $n = 1.9$ , for  $P_c = 1.5$  GPa,  $n = 1.4$ . Data for  $P_c = 1.0$  GPa from Marti et al. (2017).

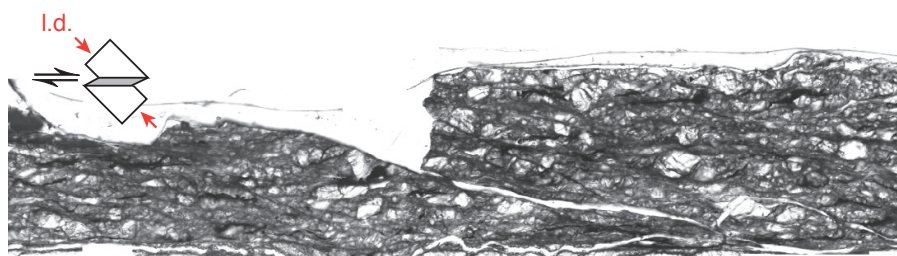


**Figure 4.** Shear zone overview. Micrograph of sample 492, plane polarized light. Strain localizes into a network of shear bands, anastomosing around low strain lenses identifiable by the large porphyroclasts. Sketch in upper left shows orientation of the micrograph with respect to the loading direction (l.d.) of the sample setup (Appendix Figure A.1).

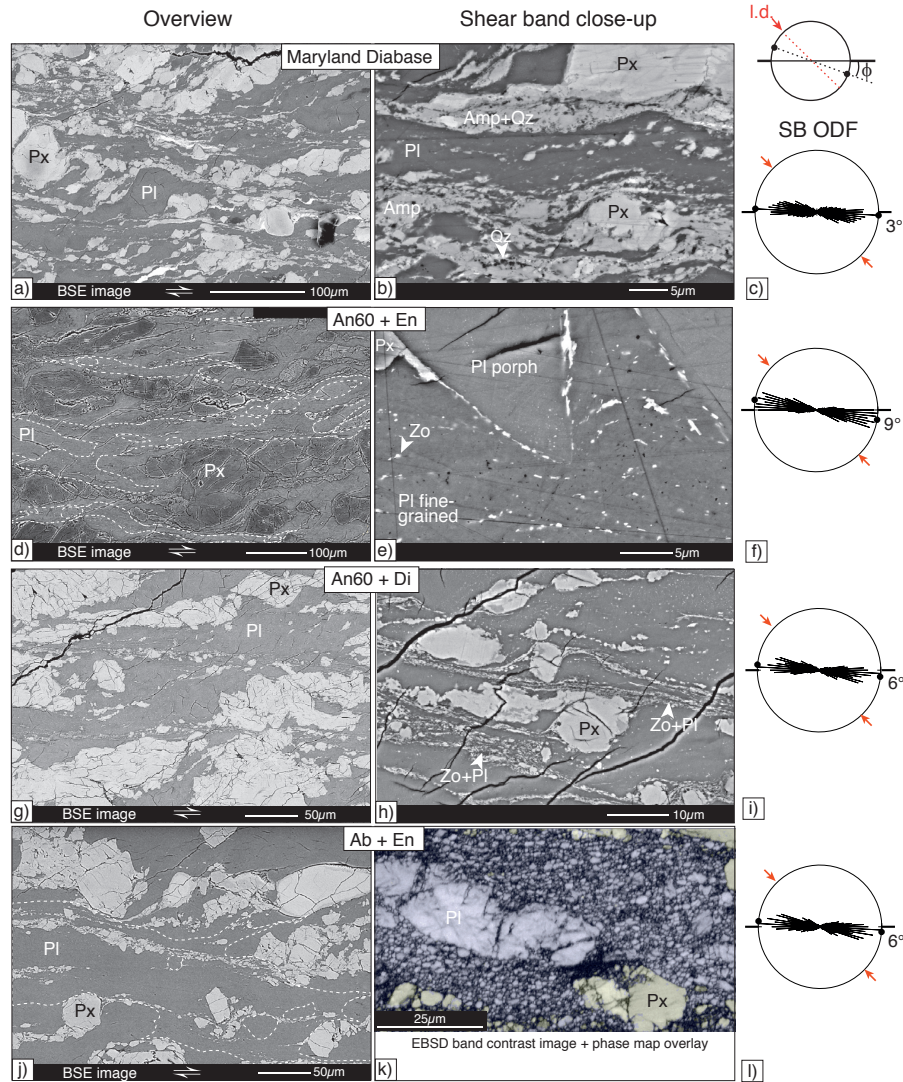


**Figure 5.** Microstructures of experiments at  $P_c \approx 1.0$  GPa. a) - c) Maryland Diabase sample material. b) Shear bands are fine-grained and often polymineralic, with the main constituents Pl, Amp and Qz. d) - f) An60+En sample material. Due to the low iron content, pyroxene appears darker than the plagioclase in BSE SEM images. In d) and j), shear bands are traced with white dotted lines. e) Fine-grained Pl + Zo in a shear band next to a Pl porphyroclast. g) - i) An60+Di sample material. j) - l) Ab+En sample material. h) EBSD band contrast image with transparent phase map overlay. Plagioclase appears blueish, pyroxene yellowish. Rose diagrams represent the orientation of the shear bands, black dots indicate preferred trend of traces. Red arrows indicate direction of loading direction. Angle,  $\phi$ , between the shear zone boundary (or forcing block) and the preferred trend is indicated.

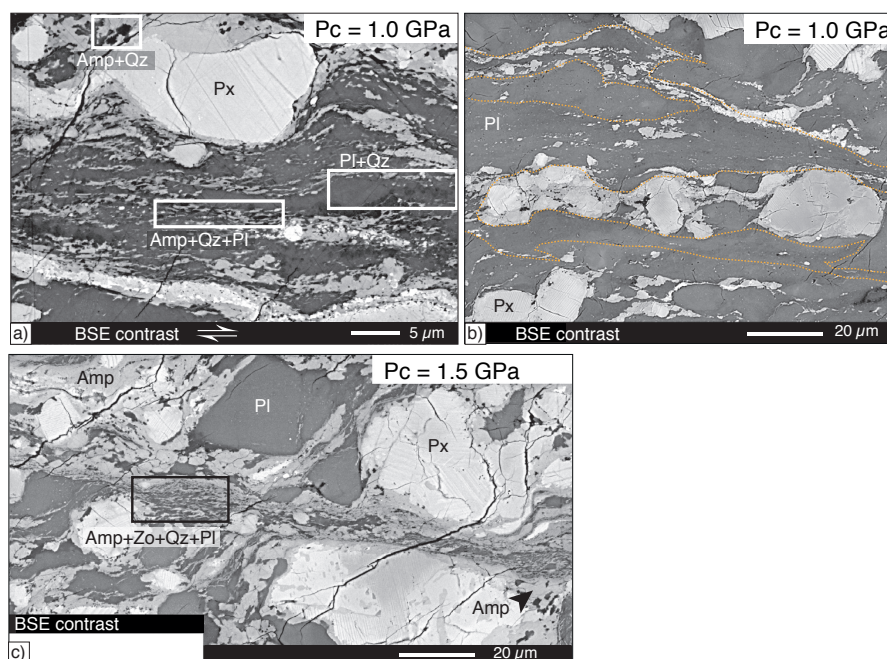


**Figure 6.** Distribution of phases in Maryland Diabase. a) Extensive phase mixing in a shear band: Mixing of Pl+Qz, Pl+Zo, and Amp+Qz. Mixing between Amp and Pl is less frequent. Px clasts show Amp coronas and asymmetric Amp tails. b) Shear bands are predominantly composed of polycrystalline Pl. c) Extensive phase mixing between Amp+Zo+Qz(+Pl) within shear bands. Px clasts show Amp coronas and asymmetric Amp tails.

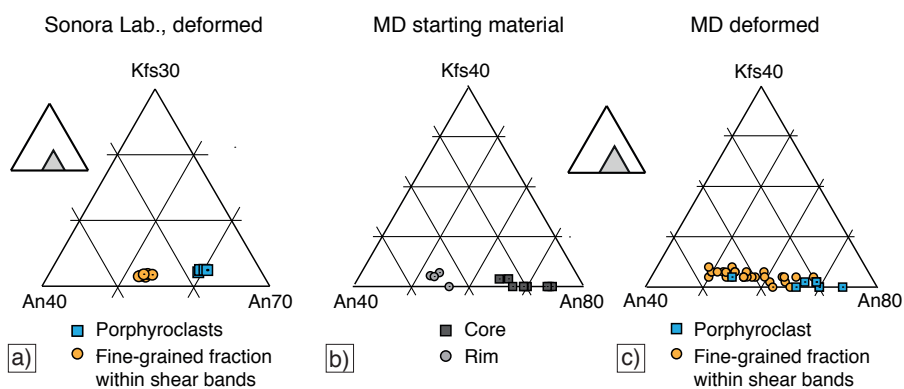


**Figure 7.** Plagioclase chemical compositions. a) Sonora Labradorite in An60+Di experiment runs. b) Maryland Diabase starting material. c) Maryland Diabase after the experiment. Porphyroclasts vs. small new grain fraction found in shear bands.

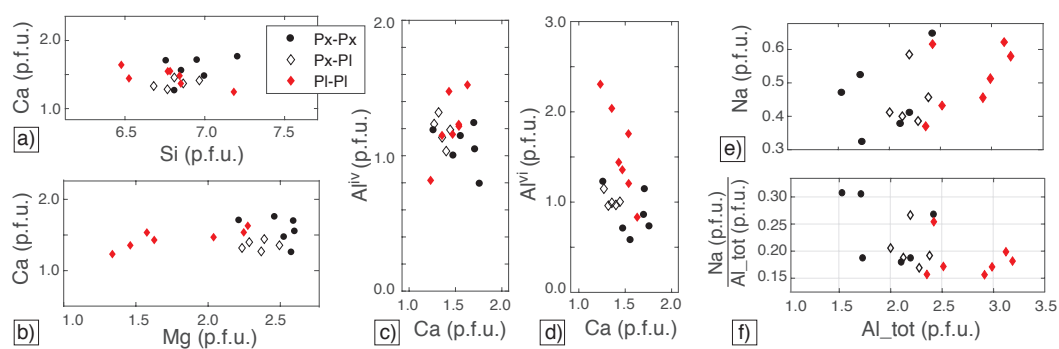


**Figure 8.** Amphibole chemistry. Amphibole grains of Maryland Diabase experiments performed at  $P_c \approx 1.0$  GPa. Measurements are grouped according to their neighbourhood: Px-Px = pyroxene dominated neighbourhood; Px-Pl = Amphibole grown between pyroxene and plagioclase grains; Pl-Pl = plagioclase dominated neighbourhood. a) Ca vs Si per formula unit (p.f.u.). b) Ca vs. Mg. c) estimated  $Al^{iv}$  vs. Ca. d) estimated  $Al^{vi}$  vs. Ca. e) Na vs. Al (total). f) Na per Al (total) ratio vs. Al (total).



**Table 3.** EDS measurements of Amp chemical compositions from samples deformed at  $P_c \approx 1.0$  GPa. Amphibole classification after Hawthorne et al. (2012). Tschermak = Tschermakite, Mg Hornbl = Magnesium Hornblende. All Fe is taken as  $Fe^{2+}$  due to the reducing conditions in the sample assembly.

normalized to 98 % wt.-%	Amphibole			
	414sm Tschermak.	414sm Mg Hornbl	490sm Mg Hornbl	490sm Tschermak.
SiO <sub>2</sub>	45.18	45.72	47.76	47.31
Al <sub>2</sub> O <sub>3</sub>	17.13	14.13	13.06	17.73
CaO	9.24	8.92	9.45	10.02
Na <sub>2</sub> O	1.63	1.74	2.12	1.84
K <sub>2</sub> O	1.26	0.86	0.89	0.90
MgO	7.56	9.95	11.24	7.39
TiO <sub>2</sub>	0.00	1.78	0.00	0.00
FeO	15.99	14.90	13.48	12.81
MnO	0.00	0.00	0.00	0.00
Cr <sub>2</sub> O <sub>3</sub>	0.00	0.00	0.00	0.00
<b>Total:</b>	<b>97.99</b>	<b>98.00</b>	<b>97.99</b>	<b>98.00</b>
Formula per 23 oxygen				
Si	6.59	6.76	6.89	6.77
Ti	0.00	0.00	0.00	0.00
Al	2.95	2.46	2.22	2.99
Fe <sup>3+</sup>	0.00	0.00	0.00	0.00
Cr	0.00	0.00	0.00	0.00
Mg	1.65	2.19	2.42	1.58
Ca	1.45	1.41	1.46	1.54
Mn	0.00	0.00	0.00	0.00
Fe <sup>2+</sup>	1.95	1.84	1.63	1.53
Na	0.46	0.50	0.59	0.51
K	0.23	0.16	0.16	0.16
<b>Total</b>	<b>15.28</b>	<b>15.34</b>	<b>15.38</b>	<b>15.08</b>

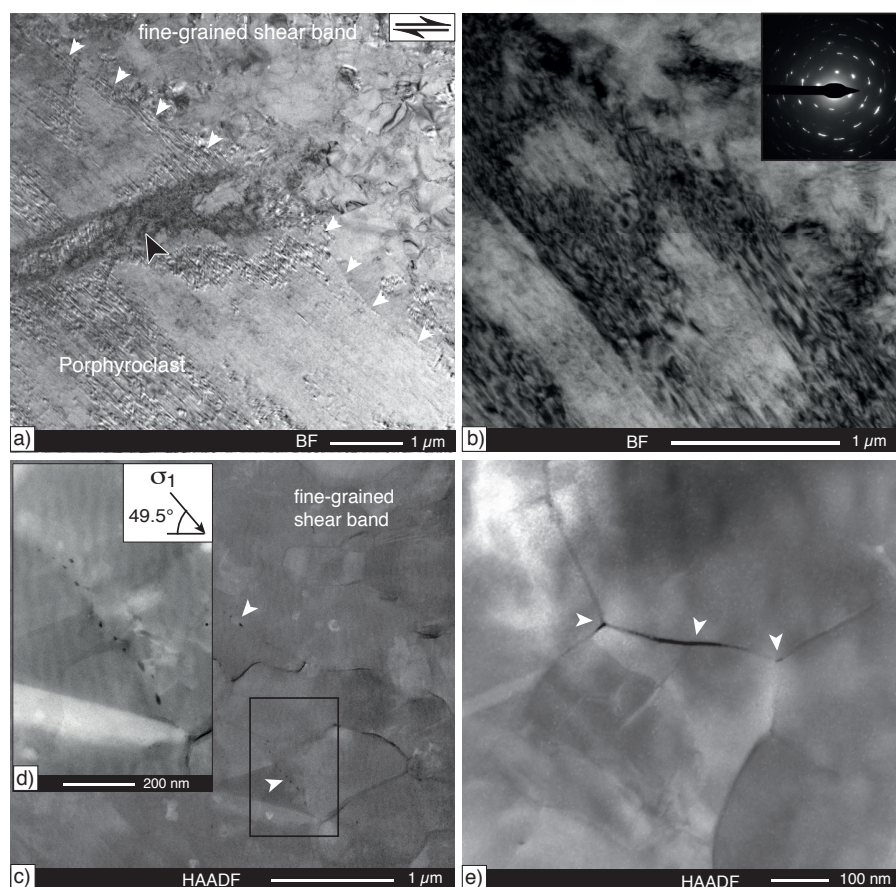


**Figure 9.** Nano-structures of shear bands in Ab+En sample. Sample (518), shear zone boundaries are horizontal, shear sense is dextral. a) Bright-field (BF) image of a plagioclase porphyroclasts adjacent to a fine grained shear band. White arrows mark the porphyroclast-shear band interface. Black arrow points to a high defect density band within the clast. b) BF image of the internal structure of porphyroclast showing high defect density. Twin lamellae run from upper left to lower right. c) HAADF image of a fine-grained plagioclase in a shear band. Black = porosity. White arrows point to open grain boundaries, black arrows indicate pore-trails along grain boundaries. Black rectangle marks close-up view in d). d) HAADF image of a pore-trail following several aligned grain boundaries. The local orientation of  $\sigma_1$  is derived from the orientation of the ISA (Table 2). e) HAADF image. White arrows point to porosity or opening sites developed along two triple-junctions and a grain boundary.

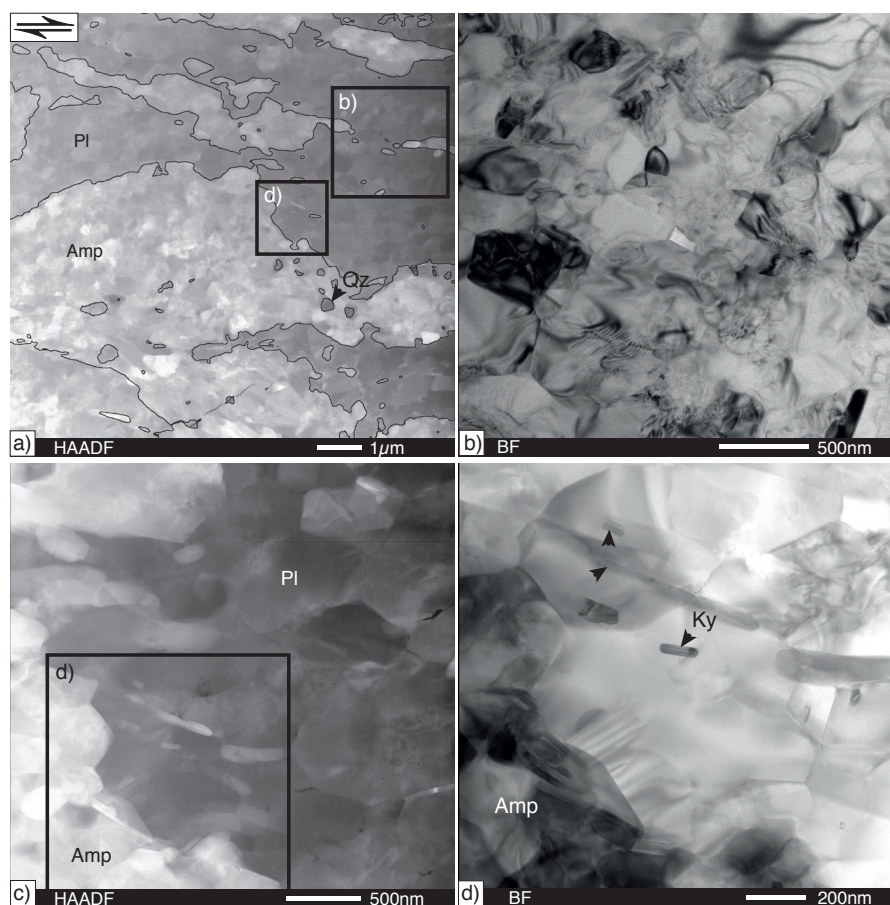


**Figure 10.** Nano structure of shear bands in Maryland Diabase sample. Sample (414), shear zone boundaries are horizontal, shear sense is dextral. a) HAADF image, overview. Amp aggregates are traced with black lines for better visibility. Rectangle indicate areas shown in b) and d). b) BF-TEM image of small (usually  $\leq 600$  nm) plagioclase grains with low internal defect densities. Grain boundaries are tight and porosity is scarce. c) HAADF image, overview. Black rectangle indicates area shown in d). d) BF-TEM image of a few Ky and Amp grains growing between Pl grains. Size of all phases is a few 100 nm, grains have a low internal defect density.

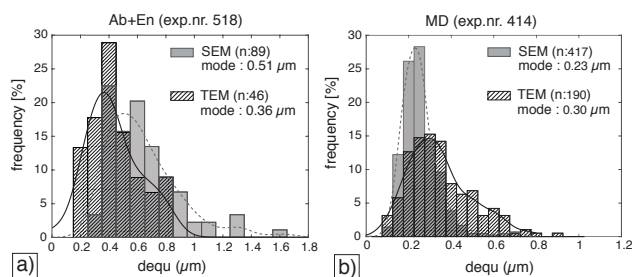


**Figure 11.** Grain size distributions of plagioclase in shear bands. a) Ab+En experiment 518, and b) the Maryland Diabase experiment 414. 2D grain size distributions (GSDs) in both samples are determined on BSE SEM images and TEM images separately. n = number of grains; solid black (TEM) and dashed grey lines (SEM) are kernel density estimate fits to the GSDs and modes determined from the fit are given in the graph.

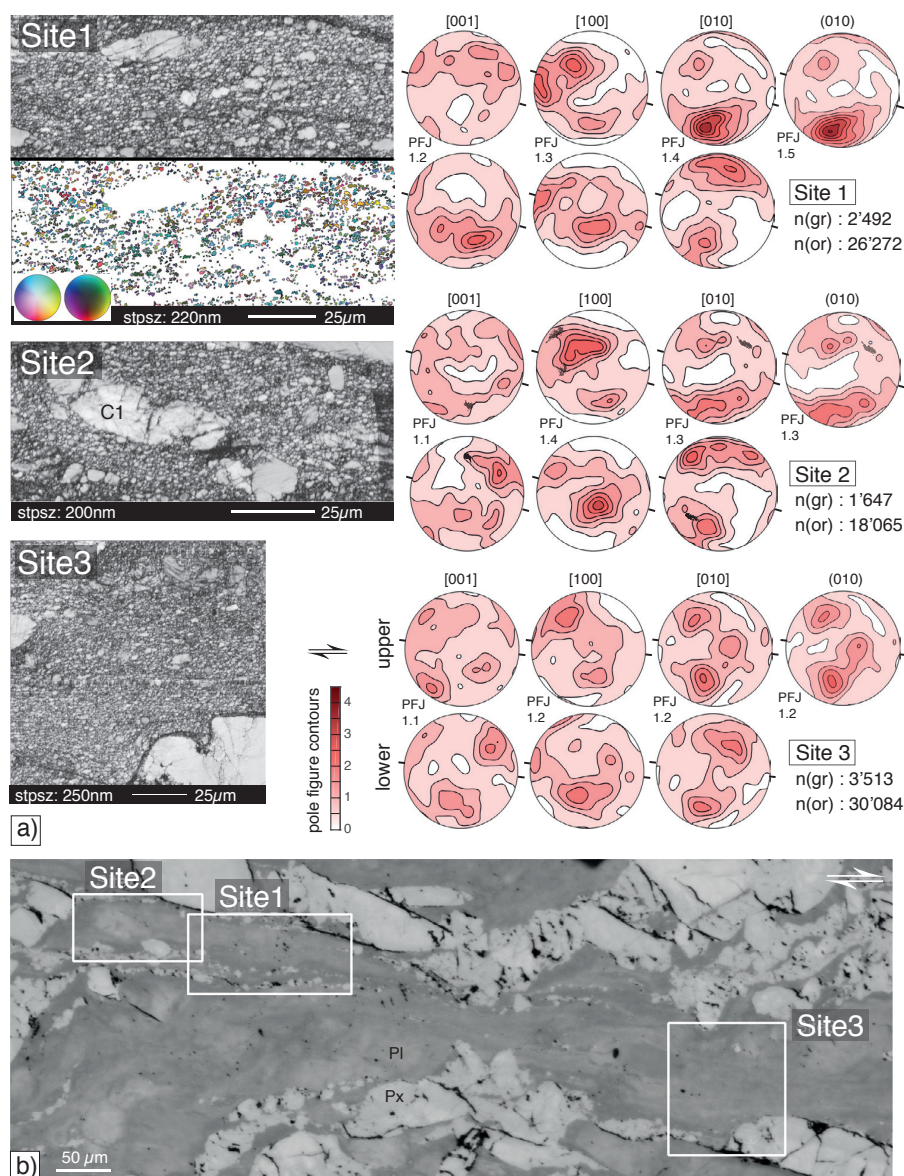


**Figure 12.** a) EBSD analysis of Ab+En sample. a) Band contrast images and contoured pole figures are given for three different sites along one shear band of sample 518 (location of maps are indicated in b). For site 1, the EBSD map (inverse pole figure coloring, x direction) is shown also. Pole figures are upper hemisphere equal angle projections of orientations from grains  $< 2 \mu\text{m}$  in diameter (and  $> 3$  pixels). For site 2, the orientation of the plagioclase porphyroclast (C1) is additionally plotted as poles (black dots) in the pole figures. Contours are at 0.5x multiples of uniform distribution. Black lines at pole figure rims indicate local shear band trend. stpsz = step size of EBSD data acquisition, n(or) = number of EBSD data points used in pole figures, and n(gr) = number of corresponding grains, PFJ = pole figure J-index, indicated at left of pole figures. b) Reflected light image. EBSD map locations are indicated, Pl = plagioclase, Px = pyroxene.

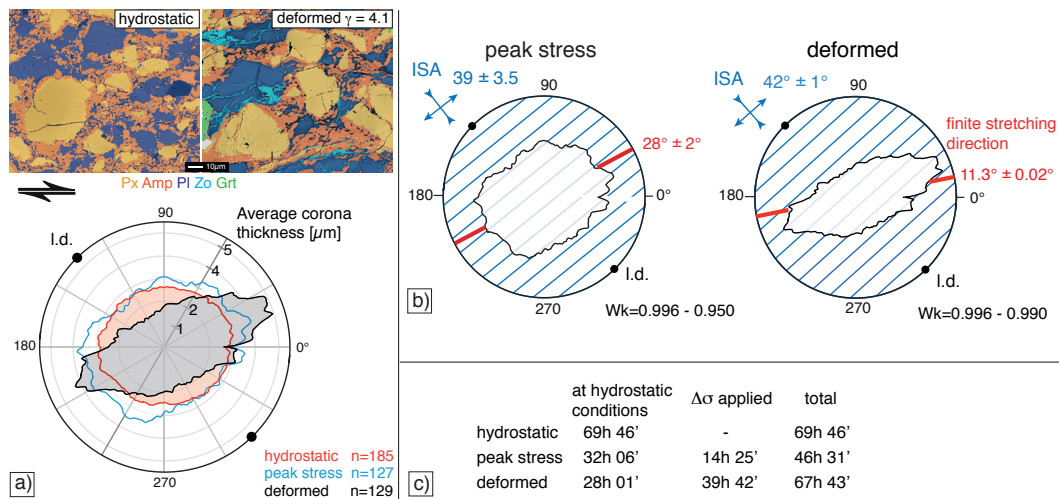


**Figure 13.** Analysis of amphibole coronas. Thickness of amphibole (Amp) corona on pyroxene (Px) porphyroclasts as a function of orientation, from Maryland Diabase experiments deformed at  $P_c \approx 1.5$  GPa. a) Average Amp corona thickness presented as rose diagram. n = number of analysed coronas. Analysis for three different samples are presented, 'hydrostatic', 'peak stress' ( $\gamma_a \sim 0.6$ ) and 'deformed' ( $\gamma_a \sim 4$ ). b) Duration of experiments in hours (h) and minutes ('). c) Kinematic analysis of a), blue lines indicate calculated instantaneous stretching directions. In red, calculated finite stretching direction. l.d. = loading direction. Wk = kinematic vorticity number. The error range in ISA direction, finite stretching direction and Wk is caused by the uncertainty of the starting thickness of the shear zone.

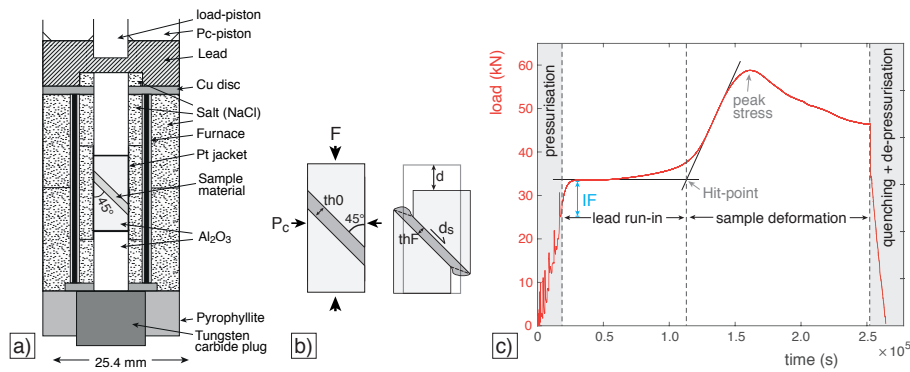


**Figure A.1.** General shear experiments. a) Sample assembly in cross-section. b) Schematic sample cross section at start of experiment (left) and after sample deformation (right).  $F$  = load induced by load-piston,  $P_c$  = confining pressure,  $d$  = axial displacement,  $d_s$  = shear displacement,  $th_0$  = shear zone thickness at start,  $th_F$  = shear zone thickness at end of experiment. c) Phases of an experiment, red line = load  $F(t)$ . During ‘pressurization’, the sample is brought to the desired  $P_c$ - $T$  conditions. Black dot denotes start of experiment. IF = initial load increase caused by machine friction. Phase 1: ‘lead run-in’, the sample not loaded. Phase 2: sample supports load and deforms. ‘Hit-point’ denotes onset of sample loading. During ‘quenching + de-pressurisation’, the load is released and the temperature brought to ambient conditions.